# Degradation Mechanisms in Solid-Oxide Fuel and Electrolyzer Cells: Analytical Description of Nickel Agglomeration in a Ni/*YSZ* Electrode

L. Kröll,[1,*] L. G. J. de Haart,[1] I. Vinke,[1] and R.-A. Eichel[1,2]

[1]*Institute of Energy and Climate Research-Fundamental Electrochemistry (IEK-9), Forschungszentrum Jülich GmbH, 52425 Jülich, Germany*

[2]*Institute of Physical Chemistry, RWTH Aachen University, 52074 Aachen, Germany*

(Received 21 October 2016; revised manuscript received 3 November 2016; published 17 April 2017)

The microstructural evolution of a porous electrode consisting of a metal-ceramic matrix, consisting of nickel and yttria-stabilized zirconia (*YSZ*), is one of the main degradation mechanisms in a solid-oxide cell (SOC), in either fuel cell or electrolyzer mode. In that respect, the agglomeration of nickel particles in a SOC electrode leads to a decrease in the electronic conductivity as well as in the active catalytic area for the oxidation-reduction reaction of the fuel-water steam. An analytical model of the agglomeration behavior of a Ni/*YSZ* electrode is proposed that allows for a quantitative description of the nickel agglomeration. The accuracy of the model is validated in terms of a comparison with experimental degradation measurements. The model is based on contact probabilities of nickel clusters in a porous network of nickel and *YSZ*, derived from an algorithm of the agglomeration process. The iterative algorithm is converted into an analytical function, which involves structural parameters of the electrode, such as the porosity and the nickel content. Furthermore, to describe the agglomeration mechanism, the influence of the steam content and the flux rate are taken into account via reactions on the nickel surface. In the next step, the developed agglomeration model is combined with the mechanism of the Ostwald ripening. The calculated grain-size growth is compared to measurements at different temperatures and under low flux rates and low steam content, as well as under high flux rates and high steam content. The results confirm the necessity of connecting the two mechanisms and clarify the circumstances in which the single processes occur and how they contribute to the total agglomeration of the particles in the electrode.

DOI: 10.1103/PhysRevApplied.7.044007

## I. INTRODUCTION

The reduction of greenhouse-gas emissions like methane or carbon dioxide can be realized by following two fundamental strategies—either by increasing the efficiency of the transformation of chemical energy to electrical energy or by generating energy from non- or low-carbon-containing resources. In that regard, solid-oxide fuel cells (SOFCs) provide a high-efficiency and low-emission electricity generator, which can be fed with both hydrogen and hydrocarbons. These characteristics reflect the argument for an increase in energy transformation efficiency, whereas the second issue can be addressed by renewable energies. Wind energy and photovoltaics are already in use and large capacities are installed. For the long-term storage of excess energy, a cost-efficient method is provided by the conversion of electrical energy to chemicals. On the other hand, the solid-oxide electrolysis cell (SOEC)—as an inverse mode of SOFC operation—allows for a high-efficiency production of hydrogen, which can be stored in suitable tanks as a chemical energy carrier [1–4].

The SOFC and the SOEC, commonly referred as solid-oxide cells (SOCs), are envisaged for decentralized and stationary applications due to their high operating temperatures 650 °C–1000 °C. Accordingly, they have to be able to run stably for at least 50 000 h, which means that the minimization of the degradation rate is of particular importance [5]. In fuel-cell mode, the oxygen is reduced at the cathode (the air electrode). The oxygen ions pass the electrolyte, react at the anode (the fuel electrode) with the oxidized hydrogen and form water molecules (Fig. 1).

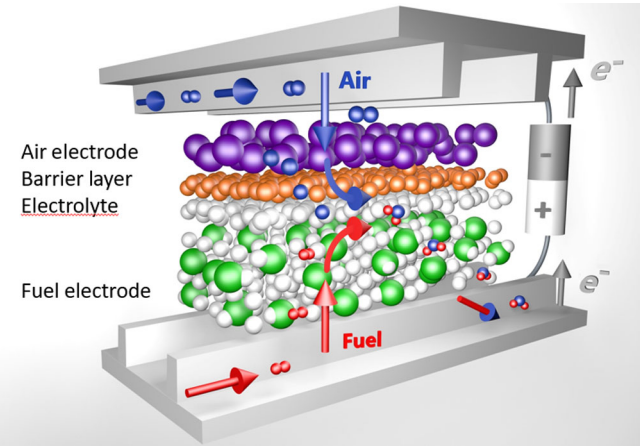


FIG. 1. Buildup of a solid-oxide cell in fuel-cell operation mode.

*L.Kroell@fz-juelich.de

 

A common choice for the fuel electrode in a SOC is a ceramic-metal composition of the electrolyte material and a transition metal, which acts as the electrocatalyst. The electrocatalyst has to be chemically stable over a wide range of oxygen partial pressures and also highly electrochemically active for the desired fuel reaction. As an electrolyte, yttria-stabilized zirconium dioxide (*YSZ*) is widely accepted. Nickel (Ni) is commonly used as transition metal in the fuel electrode due to its high abundance, relatively low costs, and high electrochemical activity [6]. This kind of electrode is well understood, but—like every material composition, to various degrees—it suffers from degradation.

In general, degradation characterizes the gradual loss of performance. As a suitable order parameter for quantifying the corresponding grade of degradation, the voltage drop is usually regarded, which occurs with long-term operation, when the cell is operated galvanostatically, i.e., under a constant current rate. The main contributions to the degradation of a fuel electrode are given by [7,8]

(1) Sulfur poisoning
(2) Coking
(3) Nickel agglomeration

Sulfur is present in small quantities in natural gas, mostly as hydrogen sulfide ($H_2S$), whereas carbon (C) can be released by reactions of hydrocarbons or carbon monoxide. Both $H_2S$ (sulfur poisoning) and C (coking), will be adsorbed at the nickel surface and can diffuse to the active catalytic area, the so-called triple-phase boundary [(TPB); Fig. 2]. In these regions the reduction or oxidation is prevented, which consequently leads to a loss in the power density. Both effects have to be avoided in gas treatment, i.e., desulphurization and water management. The third main mechanism outlines the agglomeration of Ni particles in the fuel electrode. Assuming that the zirconia particles will not change in size during the operation of the cell, the ratio of the sizes of the two involved species $r_{\mathrm{Ni}}/r_{YSZ}$ will change, which will affect

(1) the Ni surface area and, thus, for the TPB length,
(2) the electronic conductivity of the electrode since the number of electron percolation paths will decrease.

For this reason, it is of fundamental interest to predict *ab initio* the agglomeration behavior during operation in order to make a reliable lifetime prognosis of the electrode.

Faes and co-workers developed a charging-capacitor model which allows an *a posteriori* determination of the

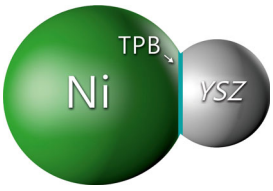


FIG. 2. Scheme of the area where the nickel, the *YSZ*, and the porous phase are in contact, which is called the triple-phase boundary.

time evolution of the Ni grain size [9,10]. Moreover, a relation of the TPB length to the Ni grain size has been derived by exploitation of the Butler-Volmer equation. The approach of Vaßen *et al.* assumed a surface-diffusion mechanism which is driven by the energy differences of the particle surfaces due to their differing mean curvatures [11]. Kennouche *et al.* presumed the surface diffusion to obey a power law [12]. Ch'ng and Pan supposed a reduction in the interfacial energy of the system as the driving force for the microstructural evolution [13]. Grain boundary and solid-state diffusivities determine the system which is initialized by two different Ni sizes at $t = 0$. In a similar manner, Chappell *et al.* investigated the influence of the particle size on the sintering rate, but instead of two distinct particle sizes, a distribution of particle sizes was considered. The calculations were kept very general and, by exchanging the specific parameters, the model could be evaluated for lattice and grain-boundary diffusion [14]. An even more sophisticated model was proposed by Wakai and Brakke [15]. The change of the shape of the agglomerates is driven by two processes: bulk migration and surface diffusion. These processes are described with the help of the surface tension and moments of inertia tensors, which allows for simulating the anisotropic effects. As starting parameters, the main axis ratio and a dimensionless relaxation time are required. Chen *et al.* performed phase-field calculations with the Cahn-Hilliard free-energy functional describing the three phases, Ni, *YSZ*, and the porous phase [16]. The time dependence is introduced by means of asymptotic analysis [17]. Deng followed a similar approach by using phase-field modeling. He emphasized the direction dependence of the diffusion [18]. Leclerc and Gelin simulated the shape and the size of distributed particles in a virtual box which is exposed to gravity, friction forces, and a van der Waals interaction [19]. Ioselevich recommended a correlated percolation model which makes use of a simulation algorithm in which the agglomeration of two neighboring particles occurs with a parametric probability which also defines the time scale of the system [20].

In Sec. II, a model of the agglomeration process of nickel spheres in a SOC fuel electrode is proposed. The derivation consists of three parts: In the first step, an agglomeration model is derived basing on the assumption that two nickel spheres can only agglomerate if they are in contact. In the second step, the mechanism of the Ostwald ripening is introduced and its impact on the microstructure of the electrode is discussed. Two possible channels for incorporating the Ostwald ripening are presented. The third part merges the agglomeration model developed at the beginning of the section with the Ostwald ripening. In Sec. III, calculations on the basis of the developed model are compared to experimental data. Section IV deals with the implications of the model, for example, whether the agglomeration is mainly driven by the sintering of two adjacent particles or by the Ostwald ripening. Furthermore,

we investigate under which circumstances which effect arises and how these effects can be minimized.

## II. STATISTICAL SINTERING MODEL

### A. Derivation of the agglomeration model

The main thrust of the model proposed here for nickel agglomeration can be characterized as follows: a sintering process will only occur when a particle has at least one chemically identical neighbor. This idea can be expressed as

$$V_{i+1} = (1 - w_i)V_i + c_i^{\text{grow}} w_i V_i \tag{1}$$

and states the growth of a particle with volume $V_i$ at a given time $t_i$. The volume in the next step, $V_{i+1}$, is composed of the former volume weighted with the probability of having no neighbor, $(1 - w_i)$, and the former volume weighted with the probability of having at least one neighbor $w_i$ times a growth factor $c_i^{\text{grow}}$. This factor has to be larger than 1; otherwise, the equation will portray a shrinkage process. Furthermore, it is expected that the growth factor is less than 2, which means that, in one step, the volume can double at the maximum. Consequently, Eq. (1) describes the sintering of two particles. In Appendix A, the time-dependent volume is derived. The result is

$$y = \frac{V}{V_0} = \left(1 + \frac{mt}{k}\right)^k, \tag{2}$$

where $m$ denotes a time constant and $k$ depends on the microstructural parameters of the investigated system. The evolution of the relative volume under different $k$ values is shown in Fig. 3. Besides the two extreme values of 0 and 1, the curves have small growth rates at large $t$, especially when the factor $k$ is small. The determination of the factor $k$ in Eq. (2) is performed in Appendix B and has a maximum at

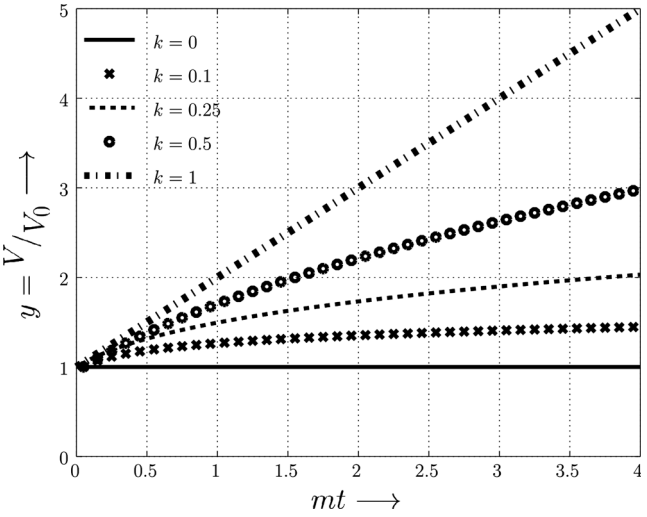


FIG. 3. Example showing the evolution of the relative volume for different values of $k$.

$$k_{\max} = \frac{3}{2\sqrt{13} + 8} \approx 0.2. \tag{3}$$

In the literature, it is stated that the length scale of a system of sintering particles $l_s$ obeys a power law of the form

$$l_s^n - l_{s,0}^n = K_D t \Rightarrow \frac{l_s}{l_{s,0}} = \left(1 + \frac{K_D t}{l_{s,0}^n}\right)^{1/n}, \tag{4}$$

with the initial scale length $l_{s,0}$ and the mass transport coefficient $K_D$. In the case of surface diffusion, the parameter is set at $n = 4$ [21], which is much smaller than

$$n = \frac{3}{k_{\max}} \approx 15, \tag{5}$$

as developed in the present model. The factor 3 in Eq. (5) takes into account the fact that Eq. (2) describes a volumetric growth process, in contrast to the length-scale growth process in Eq. (4).

In Appendix C, we demonstrate that one assumption necessary for deriving formula (2) is not valid and that the calculations have to be modified. In order to improve the time-dependent volume function, the exponential factor is taken as a function in $t$, too:

$$y = \frac{V}{V_0} = \left(1 + \frac{mt}{k(t)}\right)^{k(t)}. \tag{6}$$

The exponential factor $k$ is given by

$$k(t) = \frac{1}{1 + \alpha b} e^{[(1/2)\alpha b/(1+\alpha b)(1-e^{-2mt})]}. \tag{7}$$

The calculations are carried out in Appendix C. The change in the time evolution of the volume is displayed in Fig. 4.

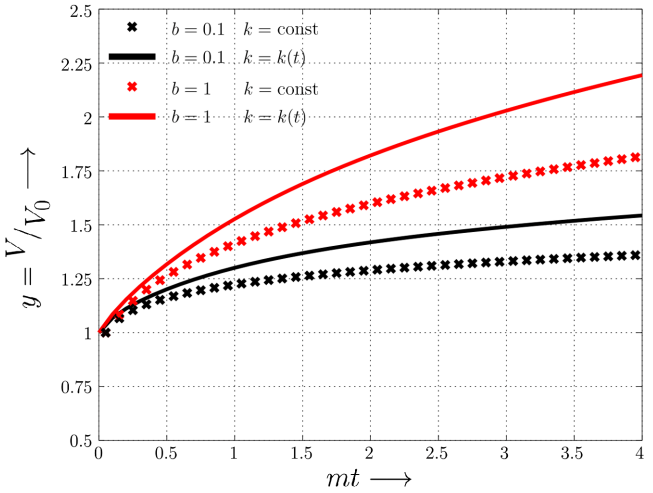


FIG. 4. Change in the volume size due to the time dependency of the exponential factor $k(t)$. The solid lines show the evolution of the particle size with the time dependency given by Eqs. (6) and (7), whereas the dotted lines describe the particle evolution under the assumption of a constant factor $k$. The factor $k$ is evaluated with $b = 0.1$ (the black lines) and $b = 1$ (the red lines).

In order to compare the model to experimental results, the parameter $b$ and its dependencies on microstructural and operating parameters have to be determined. In Appendix D, the estimation of $b$ is presented:

$$b = b_c \left| \ln\left(\frac{V_0}{V_{YSZ}}\frac{rV_{Ni}}{rV_{YSZ}}\right)\right|. \quad (8)$$

The factor $b_c$ is a global parameter which does not depend on any geometrical parameters of the system.

### B. Agglomeration due to the Ostwald ripening

By an analysis of the dimensions, the time constant $m$ can be interpreted as

$$m = \frac{D}{l^2}. \quad (9)$$

The diffusion constant $D$ depends on the underlying mechanism. Hereafter, it is assumed that the main contribution to the movement of the particles is surface-diffusion driven. Hence, the diffusion coefficient of interest is the surface-diffusion coefficient $D_s$. The length scale $l$ is unknown and has to be determined through experimental data.

A question of high interest is whether the time coefficient $m$ will change with respect to $D_s$ if the surface of the nickel is occupied by foreign molecules. Investigations of the SOFC-Life project performed in Ekaterinburg, Russia [22], show different agglomeration behaviors when atmospheric parameters, such as the flow rate of the gas and the fuel content, are changed.

General studies on heterogeneous reaction systems [23] can help to understand the elementary processes. Also, an atomistic approach involving the Coulomb interaction of charged particles can be helpful [24]. A lot of work has already been published on the reduction and oxidation kinetics on nickel surfaces involving the reaction [25–28]

$$H_2 + O^{2-} \rightleftharpoons H_2O + 2e^-. \quad (10)$$

In a SOC, the influence of the zirconia can play an important role, too [29–31]. Water-gas shift reactions and internal reformings with methane are also taken into consideration [32–35].

The approach carried out here does not take into account the kinetics of the reduction and oxidation reactions in detail, but it emphasizes the surface coverage of the nickel spheres at equilibrium.

The chemical potential of an adsorbed monolayer is

$$\frac{\mu}{RT} = \ln(\lambda_1\Theta_{Ni}) + 2\lambda_2\Theta_{Ni}, \quad (11)$$

with the ideal gas constant $R$ and the temperature $T$. The factor $\Theta_{Ni}$ stands for the surface coverage of the nickel on the nickel surface [36]. The uncovered nickel surface is $\Theta_{Ni} = (1-\Theta)$, where $\Theta$ is the surface coverage of the nickel by foreign molecules. The constants $\lambda_1$ and $\lambda_2$ depend on the temperature, the surface structure, and the kind of molecules which are adsorbed. If different species are adsorbed, the chemical potential has to be extended to

$$\frac{\mu}{RT} = \ln(\lambda_1\Theta_{Ni}) + 2\lambda_2\Theta_{Ni} + \sum_{i=0}^{n}\Gamma_i\Theta_i. \quad (12)$$

The surface coverage of the $i$th of $n$ species is denoted as $\Theta_i$. The parameters $\Gamma_i$ have the same characteristics as the constants $\lambda_1$ and $\lambda_2$ [36]. The surface-diffusion coefficient $D_s$ is expected to be influenced by the chemical potential in the following way:

$$D_s = \widetilde{D_s}e^{\mu/RT} = D_{s,0}(1-\theta)e^{2\lambda_2(1-\Theta)+\sum_{i=0}^{n}\Gamma_i\Theta_i}. \quad (13)$$

The interpretation is that only the uncovered surface provides the nickel particles the opportunity to move on the nickel surface, which leads to an agglomeration of adjacent spheres. The adsorbates can react in many different ways with the nickel (Fig. 5). The dominant reaction measured in the system Ni, $H_2$, and $H_2O$ is nickel hydroxide [$Ni(OH)_2$] [37]:

$$Ni + 2H_2O \rightleftharpoons Ni(OH)_2 + H_2. \quad (14)$$

Under this premise, the surface-coverage coefficients of the different species at equilibrium are calculated in

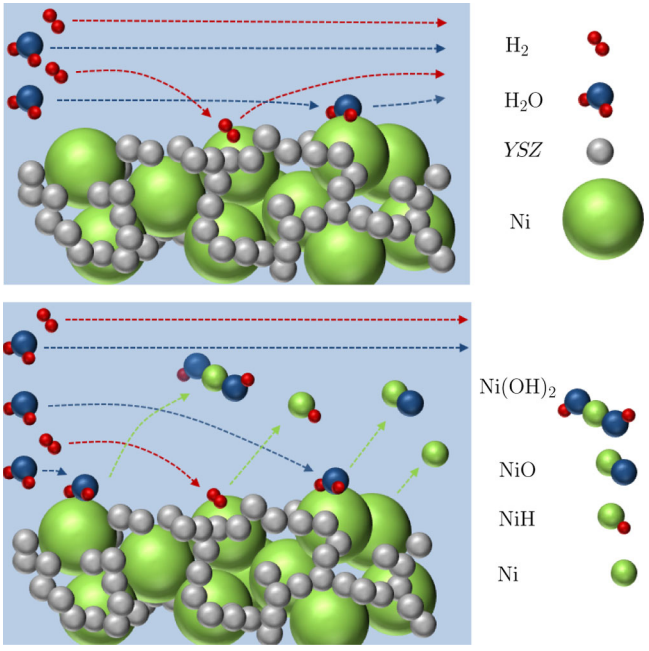


FIG. 5. Hydrogen and water can be ad- and desorbed (top panel), whereas the other molecules and atoms occur as a result of surface reactions (bottom panel).

Appendix E. These coefficients include the reaction-rate coefficients of the regarded reactions which are determined in Appendix F.

Besides the dependency of the agglomeration on the surface diffusion, the agglomeration due to ad- and desorption processes has to be studied. The desorbed $Ni(OH)_2$ can be adsorbed at a different place on the nickel surface. This mechanism leads to a second agglomeration mechanism. This effect can be observed, especially in very moist atmospheres, which are typical in solid-oxide electrolyzer cells [38] and are known as Ostwald ripening. A review on the different Ostwald-ripening theories can be found in the literature [39].

The pressure on a curved surface $p_c$ is changed compared to the pressure on a flat surface $p_p$. If the curved surface is provided by a particle with radius $r$, the Gibbs-Thomson relation holds:

$$p_c = p_p e^{(2\gamma V_{\mathrm{mol}}/RT)(1/r)} = p_p e^{l_c/r}, \tag{15}$$

where $\gamma$ denotes the surface tension, $l_c$ the critical length, and $V_{\mathrm{mol}}$ the molar volume of the spherical particle. Owing to the $r$ dependency, the pressure is higher at the surface of small particles and lower at the surface of large particles. This pressure gradient leads to a flux from the smaller to the larger particles, with the larger spheres growing at the cost of the smaller ones (Fig. 6).

It is expected that the time evolution due to the Ostwald ripening obeys the power law

$$r^3(t) - r_{\mathrm{Ni}}^3 = K_o t \Rightarrow \frac{r(t)}{r_{\mathrm{Ni}}} = \left(1 + \frac{K_o t}{r_{\mathrm{Ni}}^3}\right)^{1/3}, \tag{16}$$

as in Eq. (4), where the radius of the spheres $l_s = r(t)$ and $l_{s,0} = r_{\mathrm{Ni}}$ is taken as the characteristic length scale. The parameter $n$ is set to $n = 3$. An appropriate approach for determining the time constant $K_O$ is the Ardell [modified Lifshitz-Slyozov-Wagner (MLSW)] theory [40]. The resulting value for $K_O$ is specified in Appendix G in Eqs. (G1)–(G5).

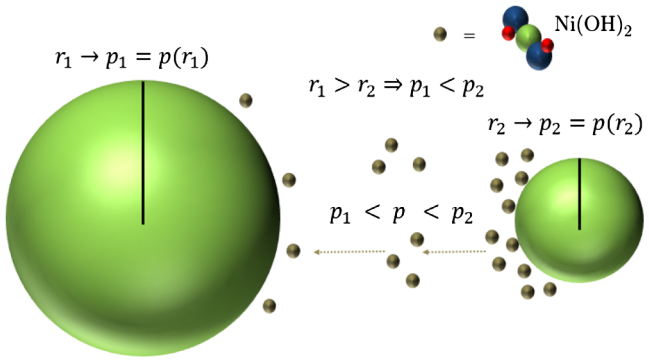


FIG. 6. The difference in the curvatures leads to a pressure gradient which acts as a driving force for nickel hydroxide molecules to migrate from smaller to larger particles.

The only free parameter is the diffusion coefficient of the Ostwald ripening, $D_{\mathrm{Ost}}$. The diffusion in a multicomponent system can be characterized with the help of the Maxwell-Stefan theory [41]. However, in the case of diluted gases, the diffusion coefficient can also be calculated by the Enskog-Landau theory [42]. The diffusion coefficient is a measure of the mobility of a species. As mentioned above, the molecules flow from regions of higher pressure to regions of lower pressure. In this model, however, all particles have the same size and, therefore, a determination of pressure differences cannot be made directly. At this point, two ways of incorporating the Ostwald ripening are introduced.

### 1. Ostwald ripening due to the fuel flow rate

In principle, the flow of the $Ni(OH)_2$ particles has to be seen as undirected. However, if a flow rate is applied, the undirected flow changes and will have a preferred orientation. The main idea is schematically drawn in Fig. 7. Thus, it is presumed that the diffusion coefficient is proportional to the flow rate:

$$D_{\mathrm{Ost}}^{\mathrm{fr}} \propto \dot{V}. \tag{17}$$

### 2. Ostwald ripening due to the deviation of the particle size

If all particles are equal in size, the deviation of the distribution vanishes. This assumption implies a constant pressure at the surfaces of the spheres over the whole sample. Hence, the pressure difference between two particles disappears and the Ostwald ripening does not take place. An appropriate way to formulate this train of thought is

$$D_{\mathrm{Ost}}^{\mathrm{der}} \propto \frac{\sigma_r}{r_{\mathrm{Ni}}}. \tag{18}$$

In the next step, the influence of the $YSZ$ particle size is recognized. The $Ni(OH)_2$ molecules can move almost freely

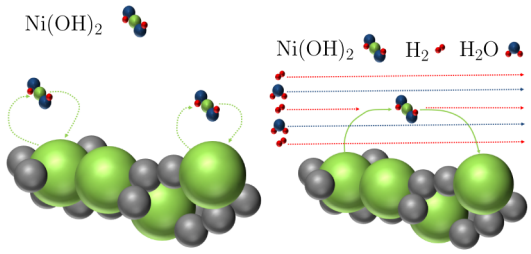


FIG. 7. The scheme shows the influence of the flow rate on the agglomeration mechanism by the Ostwald ripening. Only if a flow rate is applied do the nickel hydroxide particles move from one sphere to another (right panel); otherwise, they stay with the same particle and do not contribute to the agglomeration process (left panel).

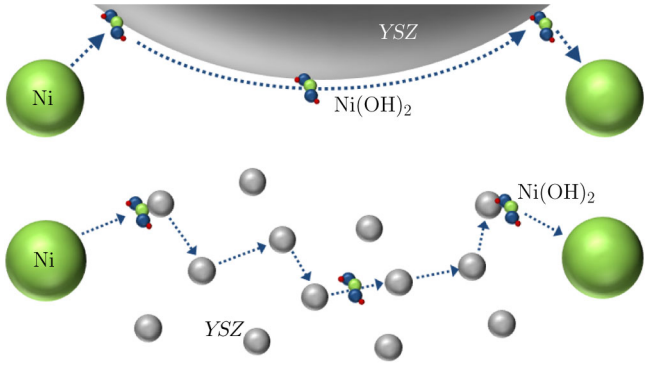


FIG. 8. The scheme shows the influence of the *YSZ* particle size on the agglomeration mechanism by the Ostwald ripening. The $Ni(OH)_2$ molecules can move more freely on the surface; thus, they can cover larger distances if the *YSZ* particles are larger. This process connects more distant particles and enables a more effective exchange between two Ni spheres.

on the surface of a *YSZ* sphere, whereas in the case of a jump between two *YSZ* spheres, an energy barrier has to be passed. Consequently, larger *YSZ* particles enable more distant Ni spheres to interact with each other, as shown in Fig. 8. The value of interest is the ratio between the two kinds of spheres,

$$D_{\mathrm{Ost}}^{\mathrm{der}} \propto \frac{r_{YSZ}}{r_{\mathrm{Ni}}}. \tag{19}$$

In Appendix H, a derivation including the influence of the atmosphere in the SOC electrode is executed. The final result of the diffusion coefficient is

$$D_{\mathrm{Ost}} = \frac{p_{\mathrm{Ni(OH)_2}}}{p_{\mathrm{H_2}} + p_{\mathrm{H_2O}}} \left( A_{\mathrm{eff}} \frac{\dot{V}}{\varepsilon V_{\mathrm{elec}}} + \frac{\sigma_r}{r_{\mathrm{Ni}}} \frac{r_{YSZ}}{r_{\mathrm{Ni}}} D_{\mathrm{Ost},0}^{\mathrm{der}} \right), \tag{20}$$

where the $p_i$'s denotes the pressure of the indicated species and $\varepsilon$ and $V_{\mathrm{elec}}$ are the porosity and the volume of the electrode. The parameters $A_{\mathrm{eff}}$ and $D_{\mathrm{Ost},0}^{\mathrm{der}}$ are free parameters and have to be specified by experimental data.

TABLE I. Parameter selection.

| $l$(m) | $b_c$ | $D_{\mathrm{Ost},0}^{\mathrm{der}}$ ($\mathrm{cm^2/s}$) | $c_0$ | $A_{\mathrm{eff}}$ ($\mathrm{m^2}$) |
|---|---|---|---|---|
| 1/60 | 13 | $1.6 \times 10^{-4}$ | $5 \times 10^{-7}$ | $1.4 \times 10^{-10}$ |

### C. Integration of the Ostwald ripening into the agglomeration model

The last step consists of combining the agglomeration model presented in the first part with the Ostwald ripening. If both processes are seen as being independent of each other, the volume function becomes

$$y = \left(1 + \frac{mt}{k}\right)^k \left(1 + \frac{K_O t}{r_{\mathrm{Ni}}^3}\right). \tag{21}$$

In principle, the Ostwald ripening can intermediate an interaction between particles which are widely spaced. However, it is expected that a particle can only influence its nearer environment. Hence, a particle with no neighbors will not contribute to the Ostwald ripening. This interpretation can be expressed with the help of the probability of having at least one neighbor $w$. Moreover, a higher growth factor $g = c^{\mathrm{grow}} - 1$ will effectively increase the influenced surrounding region. These two points can be summarized as

$$K_O \to wgK_O = \frac{b}{y} K_O, \tag{22}$$

where the definition of $b = wgy$ in Eqs. (A5) and (A8) is used. Inserting this expression into formula (21) and solving the resulting equation for $y$ leads to

$$y = \frac{1}{2}\left(1 + \frac{mt}{k}\right)^k \left(1 + \sqrt{1 + \frac{4bK_O t}{r_{\mathrm{Ni}}^3 (1 + \frac{mt}{k})^k}}\right). \tag{23}$$

Considering only the Ostwald ripening by setting $m = 0$ and evaluating the borderline cases results in

$$t \to 0\colon\ y = 1 + b\frac{K_O t}{r_{\mathrm{Ni}}^3}, \quad t \to \infty\colon\ y = \sqrt{b\frac{K_O t}{r_{\mathrm{Ni}}^3}}. \tag{24}$$

Obviously, for short times $t$, the regular formula for the Ostwald ripening occurs [see Eq. (16)], whereas on the long term, the particle size increases only with the root of $t$, not linearly.

TABLE II. Microstructural parameters.

| Experiment | $r_{\mathrm{Ni}}$ ($\mu$m) | $r_{YSZ}$ ($\mu$m) | $rV_{\mathrm{Ni}}$ (%) | $\varepsilon$ (%) | $\sigma_r$ ($\mu$m) | $V_{\mathrm{elec}}$ ($\mathrm{cm^3}$) |
|---|---|---|---|---|---|---|
| Jiang [43] | 0.77 | 0.16 | 53.4/38.2 | 23.7 | 0.28 | $2.2 \times 10^{-3}$ |
| Simwonis [44] | 1.02 | 0.60 | 24 | 40 | 0.65 | $2.4 \times 10^{0}$ |
| Ekaterinburg [22] | 0.74 | 0.44 | 53.0 | 31.2 | 0.32–0.38 | $7.7 \times 10^{-2}$ |
| Faes [9] | 0.32 | 0.27 | 30 | 20 | 0.04 | $1.3 \times 10^{-1}$ |
| Tanasini [10] | 0.32 | 0.30 | 30 | 15 | 0.01 | $2.8 \times 10^{-2}$ |

TABLE III. Atmospheric parameters.

| Experiment | $T$ (°C) | $p_{H_2}/p_0$ | $p_{H_2O}/p_0$ | $\nu$ (l/h) |
|---|---|---|---|---|
| Jiang [43] | 1000 | 0.097 | 0.03 | 0 |
| Simwonis [44] | 1000 | 0.04 | 0.03 | 0 |
| Ekaterinburg [22] | 700/800 | 0.97/0.20 | 0.03/0.80 | 1.03/5.00 |
| Faes [9] | 800 | 0.97 | 0.03 | 15–24 |
| Tanasini [10] | 850 | 0.97 | 0.03 | 7.42 |

## III. COMPARISON TO EXPERIMENTS

The system has five free parameters: $l$ arises from the surface diffusion resulting in the agglomeration of two adjacent particles. This factor enters formula (6) via the connection between the time constant $m$ and the diffusion coefficient $D_s$ in Eq. (9). The surface diffusion is also affected by the surface occupation of the Ni spheres. The proportionality factor for the chemical potential of a monolayer $\mu$ in Eq. (12) is $c_0$ (see Appendix I). The microstructural dependencies enter this process via the factor $b$ [Eq. (8)], which involves the proportional constant $b_c$. The free parameters $A_{\text{eff}}$ and $D^{\text{der}}_{\text{Ost},0}$ [Eq. (H6)] are connected to the two mechanisms of the Ostwald ripening. A more detailed discussion of the characteristics of these parameters is presented in Appendix I.

The choices of the free parameters are summarized in Table I. The microstructural and operation parameters of the five investigated experiments can be seen in Tables II and III, respectively. The calculations and the comparisons to the experiments are shown in Figs. 9–13.

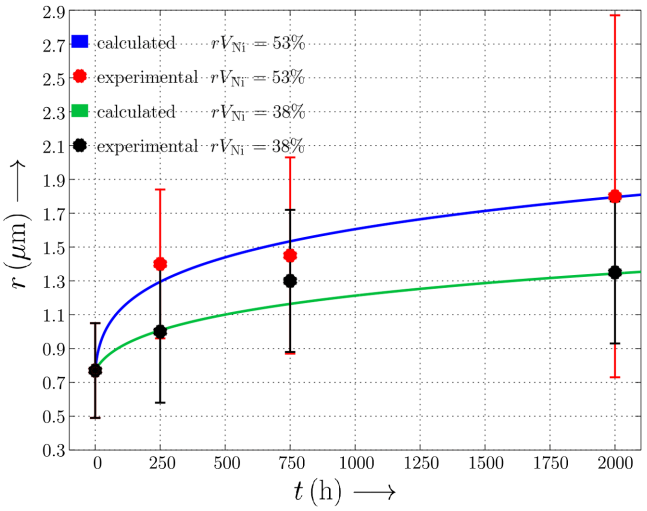


FIG. 9. Experiment performed by Jiang [43]. The dots indicate the measured particle radii $r$ in the experiment (red, $rV_{\text{Ni},1} = 0.534$; black, $rV_{\text{Ni},2} = 0.382$). The blue and green curves represent the calculated values in the time range of $t = 0$–2100 h (blue, $rV_{\text{Ni},1}$; green, $rV_{\text{Ni},2}$).

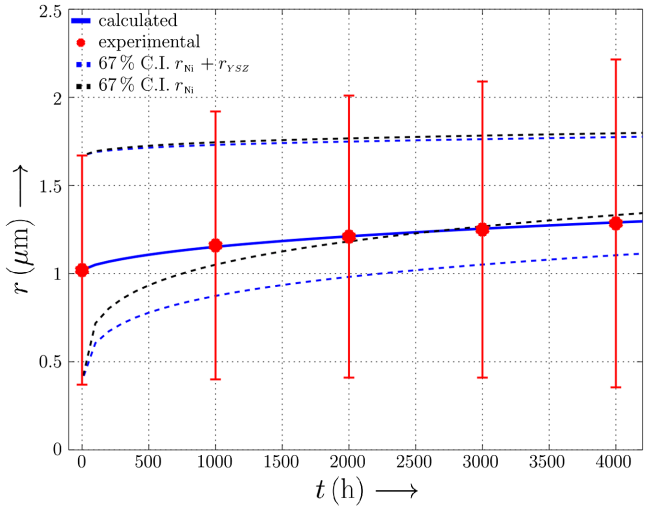


FIG. 10. Experiment performed by Simwonis [44]. The red dots are the measured particle radii $r$. The blue line represents the calculated evolution of the nickel particle size in the time range of $t = 0$–4200 h. The black dotted lines are the 67% confidence interval (C.I.) if $r_{\text{Ni}}$ is varied within the measurement error of $\sigma = 0.28$ $\mu$m. The blue dotted lines describe the 67% confidence interval if both particle sizes are varied. The input error for $r_{YSZ}$ is estimated by the assumption that the relative errors of $r_{\text{Ni}}$ and $r_{YSZ}$ are equal.

## IV. DISCUSSION

The quantitative analytical calculations of the agglomeration process are in good agreement with the experimental data (Fig. 9). The highest deviation between the calculated and measured values is observed in the experiment performed by Jiang: approximately 0.14 $\mu$m at 750 h with $rV_{\text{Ni},2}$. This value is still in the spread of the distribution which is in the range of $\sigma_r \epsilon \{0.26; 1.07\}$ $\mu$m, where the lower minimum limit is the deviation of the initial particle size and the upper limit corresponds to the deviation of the nickel size with $rV_{\text{Ni},1}$ at 2000 h.

The effects of the uncertainties of the microstructural parameters are evaluated in the calculations for the experiments performed by Simwonis and Tanasini. If the initial Ni radius $r_{\text{Ni}}$ is varied in the range of the measured uncertainties, the 67% confidence interval lies above the calculated curve, but if the $YSZ$ radius $r_{YSZ}$ is also varied, the calculated curve lies in the middle of the 67% confidence interval (Fig. 10). The relative error on $r_{YSZ}$ is set to the relative error of $r_{\text{Ni}}$. The influence of the volumetric factors $rV$ and $\epsilon$ are demonstrated in the calculations in Fig. 11. Tanasini measured four cells by image analysis. This method allows a determination of the relative errors by statistical methods. The errors are in the range approximately equal to 1%. Since the effects of an abbreviation in this region is small, the errors are multiplied by a factor of 10. Even with this magnification factor, the influence of the derivation of the parameters is not distinctive, especially in the case of nickel content. To summarize, the effects of the

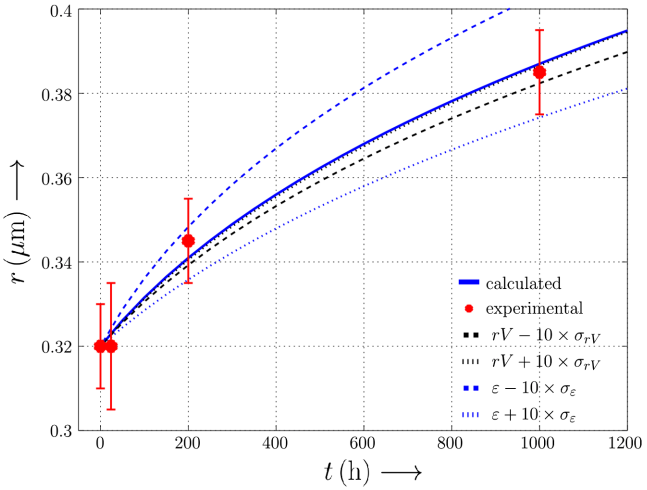


FIG. 11. Experiment performed by Tanasini [10]. The red dots are the measured particle radii $r$. The blue line represents the calculated evolution of the nickel particle size in the time range of $t = 0$–1100 h. The black and blue dotted lines are calculated with a change in the porosity $\varepsilon$ of $\pm 10\sigma_{\varepsilon}$, respectively, in relative nickel volumes $rV$ of $\pm 10\sigma_{rV}$.

particle size can be large and, moreover, can lead to unreliable results if only one particle size is varied. By contrast, changes in the volumetric parameters do not affect the particle-size evolution critically.

The influence of uncertainty in the free parameter $b_c$ is displayed in the calculations for the measurement performed by Faes. For a $b_c$ raised by 50%, the Ni particle size is decreased by approximately 0.02 $\mu$m, which lies in the range of the measured errors. In the case of a 50%-reduced value of $b_c$, the particle growth is accelerated during the first 50 h and decelerated afterwards. After 1200 h, the

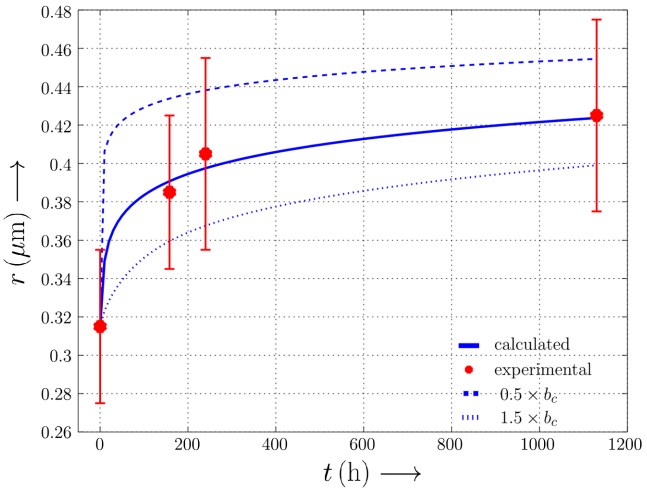


FIG. 12. Experiment performed by Faes [9]. The red dots are the measured particle radii $r$. The blue line represents the calculated evolution of the nickel particle size in the time range of $t = 0$–1200 h. The blue dotted lines are calculated with a relative change in the free parameter $b_c$ of $\pm 50\%$.

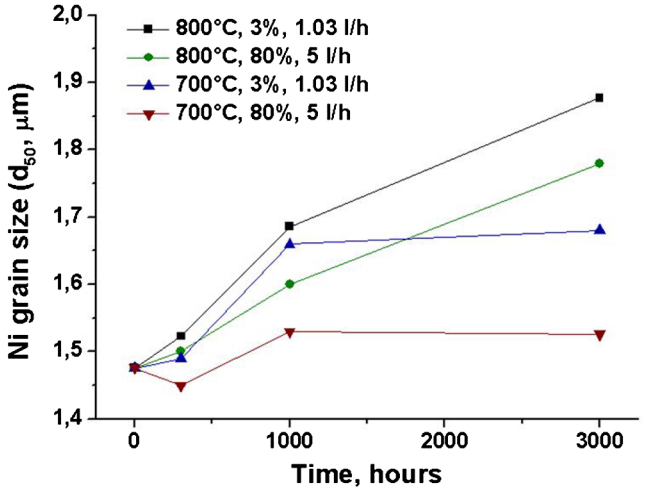


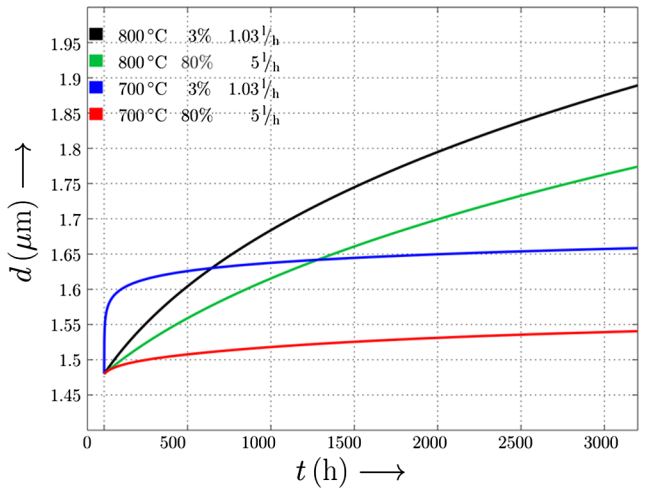


FIG. 13. (Top panel) Figure taken from Ref. [22] showing an experiment performed in Ekaterinburg. The blue and red dots are the results of the measurements at 700 °C, whereas the black and green dots represent the results of the measurement at 800 °C. The experiments are performed under the atmospheric parameters of 1.03 l/h and 97% $H_2$/3% $H_2O$ (black and blue lines) and 5l/h and 20% $H_2$/80% $H_2O$ (green and red lines). (Bottom panel) The calculated time evolution of the diameters $d$ for different temperatures and atmospheres are shown.

particle size $r_{\mathrm{Ni}}$ is approximately 0.03 $\mu$m larger than the particle size $r_{\mathrm{Ni}}$ calculated with the initial value of $b_c$.

In order to evaluate the underlying principles, the calculations are repeated; first, only the agglomeration process presented in Sec. II is taken into account and, second, only the Ostwald ripening is examined. Figures 14–18 show the results.

It can be clearly seen that both mechanisms are necessary to explain the agglomeration behavior correctly. In the experiment in Fig. 14, the Ostwald ripening is the dominant component. In Fig. 17, the developed agglomeration model based on the contact between two particles is the main process leading to an increase in the particle size. In the experiments in Figs. 15 and 16, both evolution channels

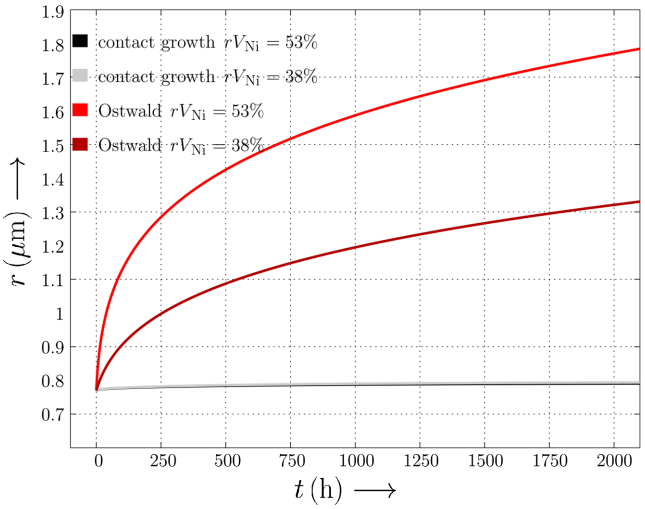


FIG. 14. Experiment performed by Jiang. The light and dark black curves indicate the agglomeration due to the merging of adjacent particles. The effect of the difference in the nickel content cannot be dissolved since the agglomeration mechanism is too weak. The light and dark red curves demonstrate the influence of the Ostwald ripening. The darker curves correspond to the lower higher content $rV_{Ni,1}$, whereas the lighter curves represent the calculations with the lower nickel content $rV_{Ni,2}$.

occur. In the first case (Fig. 15), both mechanisms contribute similarly to the agglomeration, while in Fig. 16, the Ostwald ripening has a larger effect on the agglomeration than the contact growth process. It is remarkable that the Ostwald ripening becomes stronger with increasing temperature, whereas the contact growth reaction is dominant at lower temperatures. This suggestion is confirmed when the same

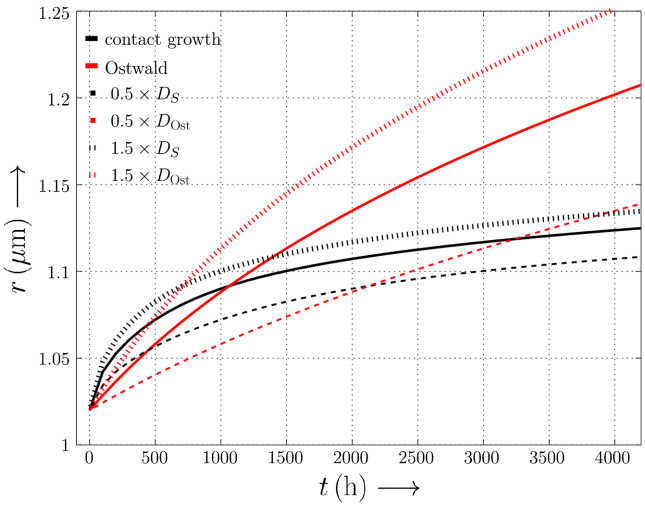


FIG. 15. Experiment performed by Simwonis. The black curve is calculated by only taking into account the agglomeration process developed in Sec. II. The red curve describes the agglomeration due to the Ostwald ripening. The dotted lines are the results of calculations with a relative change in the corresponding diffusion constant of ±50%.

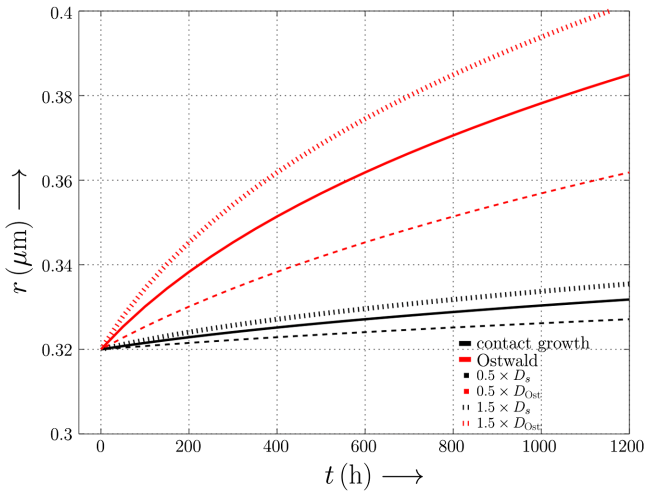


FIG. 16. Experiment performed by Tanasini. The black curve is calculated by taking into account only the agglomeration process developed in Sec. II. The red curve describes the agglomeration due to the Ostwald ripening. The dotted lines are calculated with a relative change in the corresponding diffusion constant of ±50%.

procedure is applied to the experimental system of the group in Ekaterinburg, where the samples are investigated at two different temperatures. At 800 °C, the Ostwald ripening is the underlying reason for the agglomeration, but at 700 °C, the contact growth process causes an increase in the size of the particles (Fig. 18). The two competing mechanisms also explain the nonintuitive behavior in the measurement (Fig. 13), when the size of the particles at conditions of 700 °C, 3%, 1.03 l/h increase very fast at the beginning but reach a plateau after approximately 1000 h, whereas the

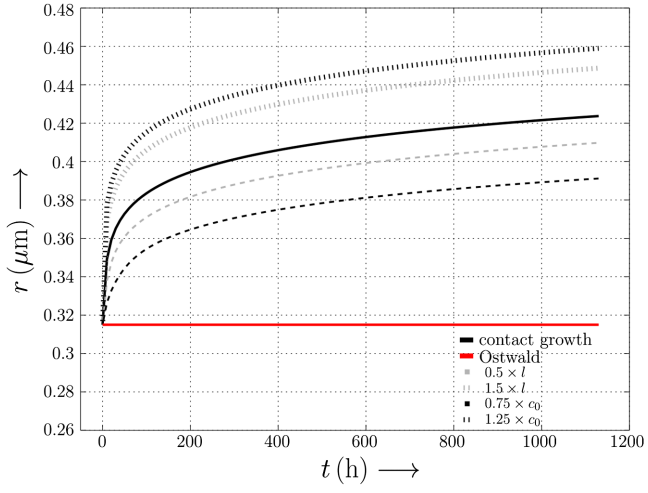


FIG. 17. Experiment performed by Faes. The black curve is calculated by taking into account only the agglomeration process developed in Sec. II. The red curve describes the agglomeration due to the Ostwald ripening. The gray dotted lines represent a variation of the free parameter $l$ by ±50%, whereas the black dotted lines are calculated with a relative change of the free parameter $c_0$ by 25%.

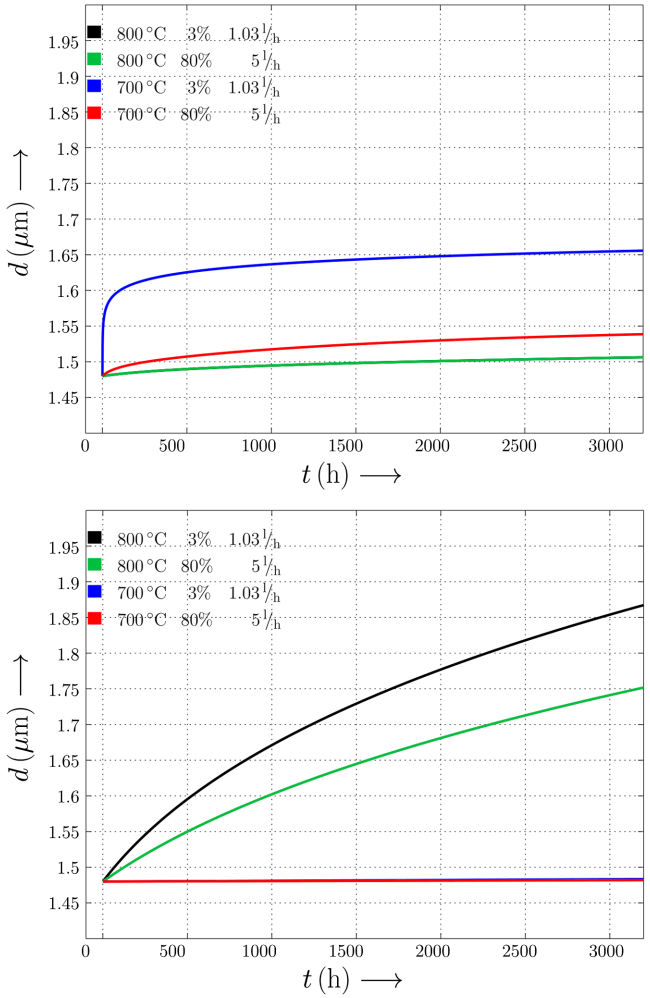


FIG. 18. Experiment performed in Ekaterinburg. (Top panel) Agglomeration due to the merging of adjacent particles. (Bottom panel) Agglomeration due to the Ostwald ripening. The black and blue curves represent the particle diameter evolution in dry atmosphere, whereas the green and red ones demonstrate the evolution in strongly humidified atmospheres. The measurements are performed at 700 °C (blue and red curves) and at 800 °C (black and green curves). The green and black curves overlap in the upper panel, while the blue and red curves overlap in the lower panel.

particle size under the conditions of 800 °C, 80%, 5 l/h seems to grow more or less linearly, leading to a smaller particle size at the first 1000 h and a larger particle size at the end of the measurement (3000 h).

The sensitivity of the calculations on the free-parameter choice is evaluated in Figs. 15–17. The diffusion constant of the contact growth mechanism $D_s$ are influenced by the free parameter $l$ and $c_0$ and the free parameters $D^{\mathrm{der}}_{\mathrm{Ost},0}$ and $A_{\mathrm{eff}}$ enters the diffusion constant of the Ostwald ripening $D_{\mathrm{Ost}}$. In Figs. 15 and 16, the diffusion constants—not the free parameters—are varied. A higher diffusion coefficient leads to a faster growth and vice versa, as is expected. The effect does not behave linearly, however. A 50% decrease in the diffusion constant has an higher impact on the particle growth than a 50% increase. The increase and the decrease of the diffusion coefficients have in common that the general characteristics of the agglomeration behavior are not changed.

By way of example, the tendency of the contact growth of a high growing rate at the beginning and a lower growing rate at the end of the measurement time compared to the growing rate of the Ostwald ripening is not substantially affected. Only specific aspects, e.g., the time at which the contribution of the Ostwald ripening becomes larger than the contribution of the contact growth, can be shifted (Fig. 15).

In the case of Ostwald ripening, the free parameters enter the diffusion constant $D_{\mathrm{Ost}}$ linearly, so a relative change of $\pm 50\%$ equates the same relative change for $D^{\mathrm{der}}_{\mathrm{Ost},0}$ and $A_{\mathrm{eff}}$. This relation is not true for the free parameters $l$ and $c_0$ since they enter the surface-diffusion constant $D_s$ in a nonlinear way ($l$ reciprocal squared, $c_0$ exponentially). The exponential dependency of $D_s$ on $c_0$ leads to a stronger change in the particle-size evolution than a change in the free parameter $l$, as can be seen in Fig. 17, where the impact of $c_0$ is stronger than the impact of $l$, even $c_0$ is varied by only $\pm 25\%$ and not by $\pm 50\%$, as in the case of $l$.

As was demonstrated in Sec. II, the Ostwald ripening is composed of two parts. One part is directly proportional to the flow rate. The second part arises from the deviation in the particle size. In the case of the measurements of Jiang and Simwonis, only the second mechanism is of interest; the first one does not occur since the flow rate is zero. As is illustrated in Fig. 17, the agglomeration in the experiment performed by Faes is exclusively driven by the contact growth process. Only in the experiments of Tansini and in Ekaterinburg does the combination of interest, a nonvanishing flow rate, and significant Ostwald ripening appear. In these experiments, both parts could potentially play a role. Subject to the experiment performed in Ekaterinburg, the Ostwald ripening is the main contribution for the higher temperature measurements (800 °C) (Fig. 18). Thus, only these measurements are considered in order to investigate the underlying reasons for the agglomeration. The Ostwald ripening is distinguished between the aforementioned two effects by setting one of the two corresponding parameters ($D^{\mathrm{der}}_{\mathrm{Ost},0}$, $A_{\mathrm{eff}}$) to zero. It reveals that, in the case of Tanasini, the Ostwald ripening is driven by the fuel-rate aspect (Fig. 19). For the experiment in Ekaterinburg, it holds that the deviation in the initial Ni size is the reason for the Ostwald ripening (Fig. 20).

The effect of the different atmospheres is also visible in the measurement in Ekaterinburg. The contact growth, as well the Ostwald ripening, is stronger in atmospheres with low humidity (Fig. 18). The measurement seems to state that the lower flow rate is correlated to a faster agglomeration, too. However, it is necessary to clarify this statement. As was already mentioned, the Ostwald ripening is explained by the deviation in the initial particle size. If the

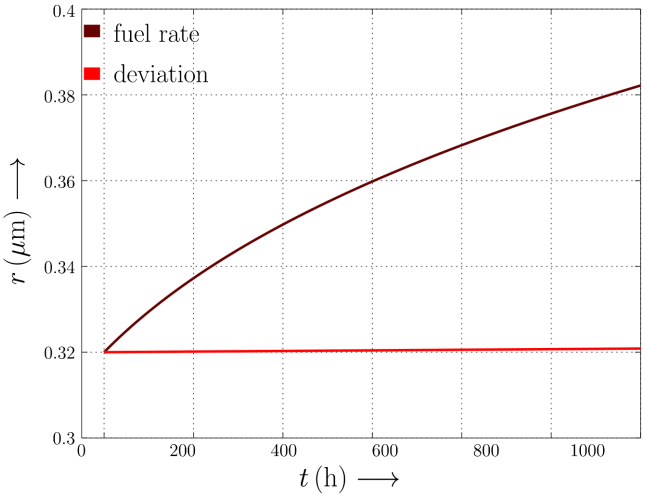


FIG. 19. The evolution due to the Ostwald ripening of the radius $r$ is shown as a function of time $t$. The dark red curve represents the agglomeration process due to the Ostwald ripening driven by the fuel rate, whereas the light red curve is calculated by assuming that only the Ostwald ripening due to the deviation mechanism occurs.

proportionality factor from the fuel-rate part [Eq. (H2)] is calculated with the help of the values in Tables II and III, it shows that this factor is almost 10 times larger for the Tanasini experiment than it is for the Ekaterinburg experiment. This behavior implies that the Ostwald ripening due to the fuel rate could become important when the fuel rate is increased accordingly. Therefore, the statement that a higher fuel rate leads to a lower agglomeration process, as seems to be the case by optically analyzing Fig. 18, does not need to be correct. It should also be noted that the determination of the free parameter $A_{\mathrm{eff}}$ is mainly based on the experiment by Tanasini, so it is not clear if this value has further dependencies on microstructural or atmospheric parameters. This uncertainty can be cleared only by incorporating the results of more data sets and by pursuing theoretical efforts.

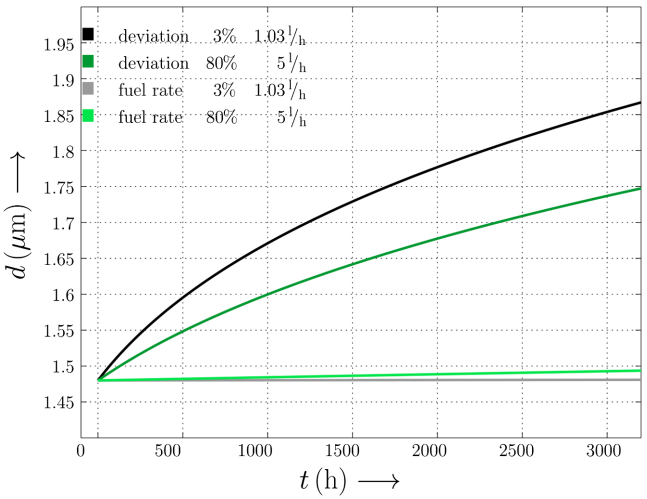


FIG. 20. The calculated time evolutions of the nickel particle diameter $d$ for the parameter setting from the experiment performed in Ekaterinburg at $T = 800\,^{\circ}\mathrm{C}$ are shown. The green curves pertain to a high humidity and flow rate, whereas the black curve represents the calculation under low humidity and flow rate. The darker curves illustrate the effect of the Ostwald ripening due to the deviation in the initial particle size and the light ones point out the influence of the flow rate on the Ostwald ripening.

Nevertheless, all mechanisms—the contact growth as well as both parts of the Ostwald ripening—can potentially play an important role and have to be considered for a full understanding of the agglomeration behavior. These results allow us to give an instruction for the conception and operation of a Ni/$YSZ$ electrode. The best choice of microstructural parameters will be achieved by setting $b = 0$, which corresponds to

$$rV_{\mathrm{Ni}}V^0 = rV_{YSZ}V_{YSZ}. \tag{25}$$

In that case, the volume will grow in a very short time period to $y_{b=0} \geq 0$, as was discussed in Sec. II. Even when the value is larger than 1, it will be a minimal value in the long term because the value is constant, whereas in the case of $b \neq 0$, the particle size will steadily grow. When quality (25) cannot be fulfilled for some reason, it is important to make the time evolution clear under operation conditions. Low temperatures decrease the influence of the Ostwald ripening at the cost of a higher contact growth process. The long-term time-evolution behavior

$$y_{\mathrm{Ost}} \propto t^{1/2} \quad \text{and} \quad y_{\mathrm{contact}} \propto t^{k}, \qquad k \leq 0.28 \tag{26}$$

indicates slower Ni particle agglomeration for the contact growth mechanism. Moreover, the Ostwald ripening can be reduced by a moderate flow rate $\nu$. For the synthesis process of the electrode, it is advantageous to produce the electrode homogeneously, which implies a low deviation of the initial particle size $\sigma_r$. Even when the condition (25) cannot be achieved, it is important to mention that the factor $b$ should be small. This conclusion becomes more important at higher temperatures, where the Ostwald ripening is dominant, as can be seen in Eq. (26).

## V. CONCLUSION

An analytical model is derived which quantitatively describes the agglomeration process in nickel/$YSZ$ electrodes of solid-oxide fuel and electrolyzer cells at different atmospheres and varying temperatures. A mechanism based on the contact probability of two adjacent particles is presented and combined with the Ostwald ripening. The contact growth process is driven by the agglomeration of two neighboring particles and, as the probability of having at least one neighbor will decrease as the particles grow, the agglomeration will be fast on short time scales and slow in

the long term. The Ostwald ripening characterizes an agglomeration mechanism due to pressure differences at the surfaces of particles differing in size. It has two manifestations. One is directly proportional to the flow rate and can be illustrated as an enforced particle flow due to the flow rate of the inlet gas. The second reason for the Ostwald ripening is the deviation of the initial particle size, which can be interpreted as a measure of the tendency of the interaction between two particles of different sizes. The combination of the contact growth model and the Ostwald ripening delivers precise and reliable results. Both models have degrees of freedom on atmospheric and microstructural parameters which are discussed and explained by first-principles methods. Nevertheless, further effort is necessary to understand the agglomeration process entirely. However, an estimation of the free parameters of the model with the help of experimental results can be performed. Since these parameters seem to be global, *ab initio* calculations are possible and, as was demonstrated, the results are in good agreement with the measured values. Furthermore, assuming the choice of the free parameter to be correct, a concrete route for the synthesis of a Ni/*YSZ* can be given. In general—and particularly at high temperatures—the ratio of the products of the initial particle size and the volumetric content of the species, Ni and *YSZ*, respectively, should be close to 1. At first glance, the agglomeration will be faster, but in the long run the particle size will be constant, which can be explained by a damped Ostwald ripening.

## APPENDIX A: CALCULATION OF THE TIME-DEPENDENT VOLUME

With the difference $\Delta V_i = V_{i+1} - V_i$, formula (1) can be rewritten as

$$\Delta V_{i+1} - \Delta V_i = g_{i+1} w_{i+1} V_{i+1} - g_i w_i V_i, \tag{A1}$$

within which the growth factor is redefined as

$$0 < g_i = c_i^{\text{grow}} - 1 < 1. \tag{A2}$$

Transforming the differences to differentials in formula (A1) leads to

$$d^2V = (g + dg)(w + dw)(V + dV) - gwV. \tag{A3}$$

The volume is a function of the time $t$, whereas the probability $w$ and the growth factor $g$ depend only on the geometry and, therefore, on the volume $V$:

$$\begin{aligned} d^2V = &\left( wV\frac{\partial g}{\partial V} + gw + Vg\frac{\partial w}{\partial V}\right)\frac{\partial V}{\partial t}dt \\ &+ \left( w\frac{\partial g}{\partial V} + g\frac{\partial w}{\partial V} + V\frac{\partial g}{\partial V}\frac{\partial w}{\partial V}\right)\left(\frac{\partial V}{\partial t}\right)^2 dt^2 \\ &+ O(dt^3). \end{aligned} \tag{A4}$$

Since the term $d^2V$ is of second order, the first-order term on the right-hand side of Eq. (A4) must vanish. Setting it to zero implies

$$\frac{d(gwV)}{dt} = 0 \Rightarrow \Delta V = gwV = b' = \text{const.} \tag{A5}$$

Using Eq. (A5) allows us to exchange $\partial g/\partial V$ and $g$ in formula (A4) with

$$\frac{\partial g}{\partial V} = -\frac{b'}{wV^2}\left(1 + \frac{V}{w}\frac{\partial w}{\partial V}\right), \qquad g = \frac{b'}{wV}, \tag{A6}$$

which leads to

$$\frac{d^2V}{dt^2} = -\frac{b'}{V^2}\left[1 + \frac{V}{w}\frac{\partial w}{\partial V} + \left(\frac{V}{w}\frac{\partial w}{\partial V}\right)^2\right]\left(\frac{\partial V}{\partial t}\right)^2. \tag{A7}$$

Normalizing the volume to the initial volume $V_0$ results in

$$\begin{aligned} y = \frac{V}{V_0} \Rightarrow \frac{d^2y}{dt^2} &= -b\alpha\left(\frac{1}{y}\frac{\partial y}{\partial t}\right)^2, \\ b = \frac{b'}{V_0}, \qquad \alpha &= 1 + \frac{y}{w}\frac{\partial w}{\partial y} + \left(\frac{y}{w}\frac{\partial w}{\partial y}\right)^2. \end{aligned} \tag{A8}$$

At this point, two assumptions are made:

(1) The contact probability will decrease if the volume grows.
(2) The change in the probability is not as strong as the change in size.

The first assumption is based on the fact that, if the contact probability increases when the size expands, the system would not be stable since, after one growing step, the tendency to agglomerate would be larger, which would lead to faster growing of the particles. The same would hold for the next step and, finally, the system would increase exponentially, which is not in accordance with the observation in the system of a SOC electrode. The second assumption is based on the presence of a decreasing probability. This guess implies that it can drop only to zero, which corresponds to a maximal relative change of 100%. By contrast, the maximum of the relative size growth can be (at least theoretically) larger than 1:

$$\begin{aligned} \left|\frac{\Delta w}{w}\right|_{\max} \approx 1, \qquad \left|\frac{\Delta y}{y}\right|_{\max} &> 1 \\ \Rightarrow 0 < \left|\frac{y}{w}\frac{\partial w}{\partial y}\right| \approx \frac{|\frac{\Delta w}{w}|_{\max}}{|\frac{\Delta y}{y}|_{\max}} &< 1. \end{aligned} \tag{A9}$$

Under these premises, the value of the function $\alpha$ [Eq. (A8)] can only be in the range of $\{3/4; 1\}$. Obviously, the value does not vary considerably. Rearranging formula (A7) with the substitution $f(y) = \ln(y)$ yields

$$\frac{d^2f}{dt^2} = -\frac{1}{k}\left(\frac{df}{dt}\right)^2, \quad \text{with} \quad k = \frac{1}{1+\frac{\alpha b}{y}}. \tag{A10}$$

The factor $\alpha$ is on the order of magnitude of 1 since the relative volume $y$ is in the range of $y\epsilon\{1;\infty\}$. Accordingly, the value of $k$ lies in the interval $\{1/1+\alpha b;1\}$. If the same holds for $b$, which we examine later, the value $k$ does not alter considerably. In order to find a solution of the differential equation (A10) which fulfills the boundary condition $y(0)=1$, the value of $k$ is taken as constant, which leads to the solution

$$f(t) = k\ln\left(\frac{k}{m}+t\right) \Rightarrow y(t) = \left(1+\frac{mt}{k}\right)^k, \tag{A11}$$

with the integration constant $m$.

For $k\epsilon\{0;1\}$, the relation with the borderline cases holds that

$$\frac{d^2y}{dt^2} < 0, \qquad y_{k=0} = 1, \qquad y_{k=1} = 1+mt. \tag{A12}$$

## APPENDIX B: CALCULATION OF THE CONSTANT EXPONENTIAL FACTOR $k$

The third root of formula (2) is the time evolution of the relative radius of the particle,

$$y^{1/3} = \left(\frac{V}{V_0}\right)^{1/3} = \frac{r}{r_0} = z = \left(1+\frac{mt}{k}\right)^{k/3}. \tag{B1}$$

If the same approach as in Eq. (1) is performed for the radius instead of the volume, the procedure is exactly the same. However, the growth factor $c^{\text{grow}}$ and the time constant $m$ are different. The time factor $m$ arises from the integration and, thus, has to be calculated from the boundary condition of the system. The probability $w$ is the same in both cases since it specifies whether two particles are in contact or not. Hence, the probability is independent of the dimension of the investigated variable. The result for the time-dependent radius of the nickel particles is

$$z = \left(1+\frac{m't}{k_z}\right)^{k_z}. \tag{B2}$$

Variables with the subscript $z$ denote the same parameters as mentioned before, but in that case they arise from the approach of the change in radius.

The comparison of Eqs. (B1) and (B2) discloses

$$\frac{k}{3} = k_z \Rightarrow 3m' = m. \tag{B3}$$

It can be proven that the link applies

$$y = z = 1 \Rightarrow 2+3\alpha b = \alpha_z b_z, \tag{B4}$$

using the parameters $\alpha$ and $b$ defined in Eq. (A8) in Appendix A.

The constants $b$ and $b_z$ are connected via the relation

$$b = \Delta y = 3z^2\Delta z = 3z^2 b_z, \tag{B5}$$

but since these are not total differentials, this expression is incorrect. Nevertheless, it is assumed that the relation holds for at least small changes in size, which can be expressed as $t=0(z=1)$. Thus, the two constants are proportional:

$$b = 3b_z. \tag{B6}$$

Combining this result with the expression in Eq. (B4) yields

$$\frac{2}{b} = \frac{1}{3}\left[1+\frac{z}{w}\frac{\partial w}{\partial z}+\left(\frac{z}{w}\frac{\partial w}{\partial z}\right)^2\right] - 3\left[1+\frac{z}{w}\frac{\partial w}{\partial z}+\left(\frac{z}{w}\frac{\partial w}{\partial z}\right)^2\right]. \tag{B7}$$

Making use of the connection

$$y = z^3 \Rightarrow dy = 3z^2dz, \tag{B8}$$

the final differential equation and its solution are given by

$$\frac{1}{b} = -\frac{4}{3} - \frac{1}{3}\frac{z}{w}\frac{\partial w}{\partial z} \Rightarrow w(z) = c_w z^{-[4+(3/b)]}. \tag{B9}$$

The constant $c_w$ is independent of the particle size. It shall be noticed that the relation for $dy$ is fully correct, in contrast to the statement in Eq. (B6), since the function in formula (B7) involves only the volume and has no direct time dependency.

By inserting the expression for $w(z)$ in Eq. (B9) into Eq. (A8), exploiting the relation (B8) yields

$$\alpha = \frac{13}{9}+\frac{5}{3}\frac{1}{b}+\frac{1}{b^2}. \tag{B10}$$

A general expression for the factor $k$ is presented in Eq. (A10) in Appendix A. Combining this equation with Eq. (B10) and setting $y=1$ finally leads to

$$k = \frac{9b}{13b^2+24b+9}. \tag{B11}$$

## APPENDIX C: CALCULATION OF THE TIME-DEPENDENT EXPONENTIAL FACTOR $k(t)$

Relation (B11) reveals that one assumption necessary for the derivation of Eq. (2) described in Appendix A is not

valid, especially for small values of $b$. Moreover, it shows that the product of $\alpha$ and $b$, both defined in Eq. (A8),) is in the interval $\{4;\infty\}$. As an example, the product is set at $\alpha b = 10$ and the exponential factors are calculated with Eq. (A10) in Appendix A:

$$\frac{y=2}{y=1} = \frac{1+10}{1+\frac{10}{2}} = 1.83. \tag{C1}$$

This calculation implies an increase of more than 80% of the exponential factor when the volume is doubled. As a consequence, the adoption of a constant exponent has to be dropped and exchanged for a time-dependent factor $k(t)$. The volume function becomes

$$y(t) = \left(1+\frac{mt}{k(t)}\right)^{k(t)}. \tag{C2}$$

The differential equation

$$y''(t) = -\frac{1}{k(t)}\left(\frac{y'(t)}{y(t)}\right)^2 \tag{C3}$$

should be fulfilled. However, since an analytical solution is not present, the second derivation is expanded in a Taylor series. All arising terms, such as

$$\left(1+\frac{mt}{k(t)}\right)^a \quad \text{and} \quad \ln\left(1+\frac{mt}{k(t)}\right), \tag{C4}$$

are exchanged for

$$y^a \quad \text{and} \quad \frac{\ln y}{k}. \tag{C5}$$

Afterwards, the volume is fixed to 1, which corresponds to an expansion at around $t = 0$. This approach leads to the differential equation (the $t$ dependency of $k$ and $y$ is dropped)

$$\begin{aligned} y'' &= m^2\left(1-t\frac{k'}{k}\right)^2 + 2\frac{k'}{k}m\left(1-t\frac{k'}{k}\right) \\ &\quad -\frac{m^2}{k}\left(1-t\frac{k'}{k}\right)^2 + 2tm\left(\frac{k'}{k}\right)^2 - 2m\frac{k'}{k} - tm \\ &= m^2\left(1-\frac{1}{k}\right)\left(1-t\frac{k'}{k}\right)^2 - mt\frac{k''}{k}. \end{aligned} \tag{C6}$$

The same procedure is carried out on the right-hand side of Eq. (C3):

$$-\frac{1}{k}\left(\frac{y'}{y}\right)^2 = -\frac{m^2}{k}\left(1-t\frac{k'}{k}\right)^2. \tag{C7}$$

Combining Eqs. (C6) and (C7) leads to

$$t\frac{k''}{k} = m\left(1-t\frac{k'}{k}\right)^2. \tag{C8}$$

At first sight, this differential equation is solved by

$$k = ct, \tag{C9}$$

with the differential constant $c$. However, inserting Eq. (C9) into Eq. (C7) leads to

$$y' = 0, \tag{C10}$$

whereas inserting Eq. (C9) into Eq. (C2) yields

$$y(t) = \left(1+\frac{m}{c}\right)^{ct}. \tag{C11}$$

A constant volume is achieved only when $c = 0$, which corresponds to a vanishing factor $k$. Hence, the solution in Eq. (C9) is not appropriate for describing the problem.

With a new function defined as

$$g(t) = t\frac{k'}{k}, \tag{C12}$$

the differential equation (C8) becomes

$$g'(t) = \frac{g(t)}{t}[1-g(t)] + m[1-g(t)]^2. \tag{C13}$$

If Eq. (C12) is investigated and the derivations are estimated by the relative change in $k$ and in the time $t$, it appears that the value of the function $g(t)$ must be small,

$$g(t) \approx \frac{\frac{\triangle k}{k}}{\frac{\triangle t}{t}} \ll 1, \tag{C14}$$

since the time is a variable which has a range of $\{0;\infty\}$, whereas $k$ will be varying only slightly in the range of $\{1/1+\alpha b;1\}$. Therefore, the relative change is very large in the case of time and very small in the case of $k$. Consequently, $g(t)$ is small and the quadratic terms in Eq. (C13) do not contribute very much. Thus, the equation can be simplified to

$$g'(t) \approx \left(\frac{1}{t}-2m\right)g(t) + m. \tag{C15}$$

The constant term $m$ is highly problematic because it implies a nonvanishing derivation for any $t$, which means that the factor $g(t)$ will never stop increasing. However, if the underlying differential equation is investigated, it can be shown that, for large values of $y$, the differential equation becomes

$$y'' + \frac{1}{k}\left(\frac{y'}{y}\right)^2 \approx k''k + \ln(y)(k')^2 = 0. \tag{C16}$$

It is obvious that a constant $k$ solves this equation. By setting $k' = 0$, Eq. (C8) is simplified to

$$t\frac{k''}{k} = 0 = m, \tag{C17}$$

which does not correspond to a constant factor $g(t)$. Even worse, it implies that the time factor $m$ has to vanish, which directly leads to a constant value of $y$. In order to avoid this problem, the differential equations are changed to

$$\begin{aligned} t\frac{k''}{k} &= m\left(1 - t\frac{k'}{k}\right)^2, \\ \rightarrow t\frac{k''}{k} &= m\left(1 - t\frac{k'}{k}\right)^2 - m, \\ \Rightarrow g'(t) &= \left(\frac{1}{t} - 2m\right)g(t) + m, \\ \rightarrow g'(t) &= \left(\frac{1}{t} - 2m\right)g(t). \end{aligned} \tag{C18}$$

The solution of this differential equation is

$$g(t) = g_0 t e^{-2mt}, \tag{C19}$$

where $g_0$ denotes an integration constant. Using the definition of $g(t)$ in Eq. (C12), the differential equation for the exponential factor $k(t)$ can be written as

$$\begin{aligned} \frac{k'(t)}{k(t)} &= g_0 e^{-2mt} \\ \Rightarrow \ln[k(t)] - \ln[k(0)] &= g_0 \int_0^t e^{-2mt'} dt' \\ \Rightarrow \ln\left(\frac{k(t)}{k(0)}\right) &= \frac{g_0}{2m}(1 - e^{-2mt}). \end{aligned} \tag{C20}$$

The integration constant $g_0$ can be evaluated by making use of the definition of $k$ in Eq. (A10),

$$\begin{aligned} k &= \frac{1}{1 + \frac{\alpha b}{y}} \Rightarrow k' = \frac{1}{1 + \frac{\alpha b}{y}} \frac{\alpha b}{y + \alpha b} \frac{1}{y} y'(t) \\ &= k \frac{\alpha b}{y + \alpha b}\left(\ln(y)\frac{k'}{k} + \frac{m(1 - t\frac{k'}{k})}{y^{\frac{1}{k}}}\right). \end{aligned} \tag{C21}$$

Setting $t = 0$ and $y = 1$, we get

$$\frac{k'(0)}{k(0)} = g_0 = m\frac{\alpha b}{1 + \alpha b}. \tag{C22}$$

Finally, the exponential factor becomes

$$k(t) = \frac{1}{1 + \alpha b} e^{[(1/2)\alpha b/(1+\alpha b)(1 - e^{-2mt})]}. \tag{C23}$$

## APPENDIX D: DETERMINATION OF THE FACTOR $b$

As described in Eqs. (A5) and (A8), the factor $b$ is proportional to the change in the relative volume $y$. The question of interest is, how does it change under a variation of a parameter such as the nickel content $rV_{\mathrm{Ni}}$, the porosity $\varepsilon$, or the starting size of the Ni and $YSZ$ particles, $V_0$ and $V_{YSZ}$? The parameter $b$ is defined as

$$b = \frac{\Delta V}{V_0}. \tag{D1}$$

When all parameters, including the time $t$ (except for the initial value $V_0$), are set as constant, a shift in $V_0$ implies a change of $b$:

$$\Delta b \propto \frac{\Delta V_0}{V_0} \Rightarrow b \propto \ln(V_0). \tag{D2}$$

If the nickel content is slightly shifted under the same restrictions, the change in $b$ can be expressed as

$$\Delta b \propto \frac{\Delta V_0}{V_0} \propto \frac{\Delta r V_{\mathrm{Ni}}}{r V_{\mathrm{Ni}}} \Rightarrow b \propto \ln(r V_{\mathrm{Ni}}). \tag{D3}$$

Combining Eqs. (D2) and (D3) leads to

$$b \propto \ln(V_0) + \ln(r V_{\mathrm{Ni}}) = \ln(V_0 r V_{\mathrm{Ni}}). \tag{D4}$$

Because of the argument that the logarithm has to be dimensionless and since the only corresponding size in the system, which is well defined, is the size of the $YSZ$ particles $V_{YSZ}$, the term (D4) has to be changed. Moreover, in order to guarantee symmetry between the nickel and the $YSZ$ particles, the volumetric $YSZ$ content $rV_{YSZ}$ is incorporated as well,

$$b = b_c \ln\left(\frac{V_0}{V_{YSZ}}\frac{r V_{\mathrm{Ni}}}{r V_{YSZ}}\right), \tag{D5}$$

where $b_c$ is a global parameter which does not depend on any geometrical parameter of the system. A value of $b$ larger than zero ensures the proper behavior of the time evolution of the nickel size. This behavior can be implemented by applying the absolute value function to expression (D5):

$$b = b_c \left| \ln\left(\frac{V_0}{V_{YSZ}}\frac{r V_{\mathrm{Ni}}}{r V_{YSZ}}\right) \right|. \tag{D6}$$

If the same line of argument were performed for the change of the relative radius $z$, steps (D2)–(D6) would have to be replaced by

$$\Delta b_z \propto \frac{\Delta r_0}{r_0} \propto \frac{\Delta V_0^{1/3}}{V_0^{1/3}} \propto \frac{\Delta r V_{\mathrm{Ni}}^{1/3}}{r V_{\mathrm{Ni}}^{1/3}}$$
$$\Rightarrow b_z = b_c \left| \ln\left[ \left(\frac{V_0}{V_{YSZ}}\right)^{1/3} \left(\frac{r V_{\mathrm{Ni}}}{r V_{YSZ}}\right)^{1/3} \right] \right|$$
$$= \frac{1}{3} b_c \left| \ln\left( \frac{V_0}{V_{YSZ}} \frac{r V_{\mathrm{Ni}}}{r V_{YSZ}} \right) \right| = \frac{1}{3} b. \quad \text{(D7)}$$

The relation between $b$ and $b_z$ which is predicted by Eq. (B6) becomes directly visible.

## APPENDIX E: INFLUENCE OF SURFACE REACTIONS

In general, particles in an atmosphere can be ad- and desorbed on the surface of solids. Depending on the tendency of being ad- or desorbed, the surface will be partially or completely covered by adsorbates. One approach facing this problem is based on the Langmuir theory [45]. Its basic assumptions are as follows: every site on the surface is identical and equivalent, the particles form only monolayers on the surface, and the adsorption rate is proportional to the nonoccupied surface $(1-\Theta)$. This train of thought can be summarized in a differential equation of the form

$$\frac{d\Theta_i}{dt} = k_{a,i}(1-\Theta) - k_{d,i}\Theta_i, \quad \text{(E1)}$$

with the total coverage $\Theta = \sum \Theta_i$ consisting of the sum over the coverage of every component and the absorption and desorption coefficients of the regarded species being $i$, $k_{a,i}$, and $k_{d,i}$.

Expecting that reactions (10) and (14) occur with rate-reaction coefficients $k_j$ and $K$ and when only $H_2$ and $H_2O$ are in the cell, all of the reactions can be summarized in a matrix format as follows:

$$\frac{d}{dt}\begin{pmatrix} \Theta_{\mathrm{H_2}} \\ \Theta_{\mathrm{H_2O}} \\ \Theta_{\mathrm{Ni(OH)_2}} \end{pmatrix} = \begin{pmatrix} k_{a,\mathrm{H_2}} \\ k_{a,\mathrm{H_2O}} \\ 0 \end{pmatrix} - \begin{pmatrix} k_{a,\mathrm{H_2}} + k_{d,\mathrm{H_2}} + k_j & k_{a,\mathrm{H_2}} - K & k_{a,\mathrm{H_2}} \\ k_{a,\mathrm{H_2O}} - k_j & k_{a,\mathrm{H_2O}} + k_{d,\mathrm{H_2O}} + 2K & k_{a,\mathrm{H_2O}} \\ 0 & -K & k_{d,\mathrm{Ni(OH)_2}} \end{pmatrix} \begin{pmatrix} \Theta_{\mathrm{H_2}} \\ \Theta_{\mathrm{H_2O}} \\ \Theta_{\mathrm{Ni(OH)_2}} \end{pmatrix}. \quad \text{(E2)}$$

This differential equation can be solved only with great effort, but if merely the equilibrium state is of interest, it is sufficient to set the left side to zero since, at equilibrium, the coverage for each species is constant. The solutions are

$$\Theta^*_{\mathrm{H_2}} = k_{d,\mathrm{Ni(OH)_2}} \frac{k_{a,\mathrm{H_2}}(k_{d,\mathrm{H_2O}} + 2K) + k_{a,\mathrm{H_2O}}K}{\mathrm{den}},$$
$$\Theta^*_{\mathrm{H_2O}} = k_{d,\mathrm{Ni(OH)_2}} \frac{k_{a,\mathrm{H_2O}}(k_{d,\mathrm{H_2}} + k_j) + k_{a,\mathrm{H_2}}k_j}{\mathrm{den}},$$
$$\Theta^*_{\mathrm{Ni(OH)_2}} = \frac{K}{k_{d,\mathrm{Ni(OH)_2}}} \Theta^*_{\mathrm{H_2O}}, \quad \text{(E3)}$$

where the denominator den in Eq. (E3) is

$$\begin{aligned} \mathrm{den} = {} & k_{d,\mathrm{Ni(OH)_2}} K(2k_{a,\mathrm{H_2}} + k_{a,\mathrm{H_2O}} + 2k_{d,\mathrm{H_2}} + k_j) \\ & + k_{d,\mathrm{Ni(OH)_2}}(k_{a,\mathrm{H_2O}}k_{d,\mathrm{H_2}} + k_{a,\mathrm{H_2}}k_{d,\mathrm{H_2O}} + k_{d,\mathrm{H_2}}k_{d,\mathrm{H_2O}}) \\ & + K(k_{a,\mathrm{H_2O}}k_{d,\mathrm{H_2}} + k_{a,\mathrm{H_2}}k_j + k_{d,\mathrm{H_2O}}k_j) \\ & + k_{d,\mathrm{Ni(OH)_2}}k_j(k_{a,\mathrm{H_2}} + k_{a,\mathrm{H_2O}} + k_{d,\mathrm{H_2O}}). \end{aligned} \quad \text{(E4)}$$

If the reaction (14) is completely suppressed, which means $K = 0$, and a zero current is applied $(j = 0 \Rightarrow k_j = 0)$, the surface coverages at equilibrium become

$$\Theta^*_{\mathrm{H_2}} = \frac{\frac{k_{a,\mathrm{H_2}}}{k_{d,\mathrm{H_2}}}}{1 + \frac{k_{a,\mathrm{H_2}}}{k_{d,\mathrm{H_2}}} + \frac{k_{a,\mathrm{H_2O}}}{k_{d,\mathrm{H_2O}}}},$$
$$\Theta^*_{\mathrm{H_2O}} = \frac{\frac{k_{a,\mathrm{H_2O}}}{k_{d,\mathrm{H_2O}}}}{1 + \frac{k_{a,\mathrm{H_2}}}{k_{d,\mathrm{H_2}}} + \frac{k_{a,\mathrm{H_2O}}}{k_{d,\mathrm{H_2O}}}},$$
$$\Theta^*_{\mathrm{Ni(OH)_2}} = 0, \quad \text{(E5)}$$

which is the result predicted by the extension of the Langmuir theory for multicomponent systems [46] when $k_{a,i}$ is replaced by $k_{a,i}p_i$.

## APPENDIX F: DETERMINATION OF THE REACTION RATE COEFFICIENTS $k_i$

The adsorption reaction-rate coefficient of species $i$ in Eq. (E1) can be calculated with the help of the Langmuir-Hertz equation [47,48]

$$k_{a,i} = \frac{p_i}{\sigma_0 \sqrt{2\pi M_i^{\mathrm{mol}} RT}}, \quad \text{(F1)}$$

with the partial pressure $p_i$ and the molar mass $M_i^{\mathrm{mol}}$ of species $i$, the ideal gas constant $R$, the absolute temperature $T$, and the number of adsorption centers per unit of surface area $\sigma_0 = 2.6 \times 10^{-9}$ mol/cm$^2$ [49]. The partial pressure of the $H_2$ and $H_2O$ are usually predetermined by the operation parameters (e.g., $H_2$, 97%; $H_2O$, 3%).

TABLE IV. Thermodynamic data for gas-phase ($g$) and surface species (Ni) at 973 K [26].

| Species | $H$(kJ/mol) | $S$(J/K mol) |
|---|---|---|
| $H_2O(g)$ | −217 | 222 |
| $H_2(g)$ | 20 | 156 |
| $H_2O$(Ni) | −273 | 130 |
| H(Ni) | −32 | 41 |

In general, the reverse reaction-rate coefficient is connected via

$$k_{d,i} = k_{a,i} e^{\Delta G/RT}, \tag{F2}$$

where $\Delta G$ denotes the Gibbs free energy of the considered reaction. The Gibbs free energy for the adsorption of $H_2O$ can be determined with the help of the thermodynamic data in Table IV:

$$\Delta G_{\text{ads}}^{H_2O} = 56\frac{\text{kJ}}{\text{mol}} - T \times 92\frac{\text{J}}{\text{K mol}}. \tag{F3}$$

In the case of $H_2$, the thermodynamic values of the adsorbed species have to be multiplied by 2 because one $H_2$ molecule is transformed into two H atoms. Nevertheless, this multiplication is not sufficient since the two molecules have to overcome the dissociation barrier which is expressed by the dissociation enthalpy $H_{\text{diss}}$ and the dissociation entropy $S_{\text{diss}}$,

$$\Delta G_{\text{ads}}^{H_2} = \left(-44\frac{\text{kJ}}{\text{mol}} + H_{\text{diss}}\right) - T \times \left(74\frac{\text{J}}{\text{K mol}} + S_{\text{diss}}\right). \tag{F4}$$

The values for the dissociation enthalpy and entropy are $H_{\text{diss}} = 436$ kJ/mol and $S_{\text{diss}} = 131$ J/K mol [50].

The Gibbs free energy for the desorption of $Ni(OH)_2$ is [51]

$$\Delta G_{\text{des}}^{Ni(OH)_2} = -240\frac{\text{kJ}}{\text{mol}} + T \times 33\frac{\text{J}}{\text{K mol}}. \tag{F5}$$

For the $Ni(OH)_2$ species, no initial partial pressure is available. Hence, $Ni(OH)_2$ is assumed to be at equilibrium with the solid and gas phases which correspond to the saturation pressure in Eq. (H5).

Besides the adsorption and desorption reaction rates, the coefficients for the $H_2/H_2O$ transformation $k_j$ [Eq. (10)] and for the production of $Ni(OH)_2$ $K$'s [Eq. (14)] are necessary for evaluating formulas (E3) and (E4). The particle flux of $H_2/H_2O$ is connected to the current density $j$ in a SOC electrode via the relation

$$\dot{n}_{H_2 \leftrightarrow H_2O} = \frac{jA}{n_{e^-}F}. \tag{F6}$$

The cross-section area of the cell is denoted by $A$, $F$ is the Faraday constant, and $n_{e^-}$ is the number of the involved electrons (here, $n_{e^-} = 2$). The sites for molecules on the nickel surface are

$$n_{\text{tot}} = \sigma_0 A_{\text{Ni}}^{\text{tot}}. \tag{F7}$$

The total surface area is

$$A_{\text{Ni}}^{\text{tot}} = A_{\text{Ni}} n_{\text{Ni}}^{\text{tot}} = 4\pi r_{\text{Ni}}^2 \frac{V_{\text{Ni}}}{\frac{4}{3}\pi r_{\text{Ni}}^3} = 3V_{\text{elec}}\frac{rV_{\text{Ni}}}{r_{\text{Ni}}}. \tag{F8}$$

The nickel volume in the electrode is given by the total electrode volume times the relative nickel content $V_{\text{Ni}} = rV_{\text{Ni}}V_{\text{elec}}$. Thus, the rate of change for the surface is

$$k_j = \frac{\dot{n}_{H_2 \leftrightarrow H_2O}}{n_{\text{Ni}}^{\text{tot}}} = \frac{r_{\text{Ni}} j}{6FrV_{\text{Ni}}l_{\text{elec}}}, \tag{F9}$$

with a thickness of the functional layer of the electrode $l_{\text{elec}}$.

The Gibbs free energy for the reaction

$$\text{Ni(Ni)} + 2H_2O(g) \rightarrow Ni(OH)_2(g) + H_2(g) \tag{F10}$$

is given by [51,52]

$$\Delta G_{\tilde{R}} = 244\frac{\text{kJ}}{\text{mol}} - T \times 25\frac{\text{J}}{\text{K mol}}. \tag{F11}$$

The abbreviation in the brackets labels whether the particle is in the gas phase ($g$) or on the nickel surface (Ni). However, in the system mentioned above, the reaction of interest is

$$\text{Ni(Ni)} + 2H_2O\text{(Ni)} \rightarrow Ni(OH)_2\text{(Ni)} + H_2\text{(Ni)}, \tag{F12}$$

with the corresponding Gibbs free energy $\Delta G_R$. The reaction (F10) is composed of the following reactions.

(i) Adsorption of $H_2O$: $\Delta G_{\text{ads}}^{H_2O}$.
(ii) Production of $Ni(OH)_2$: $\Delta G_R$.
(iii) Desorption of $H_2$: $\Delta G_{\text{des}}^{H_2} = -\Delta G_{\text{ads}}^{H_2}$.
(iv) Desorption of $Ni(OH)_2$: $\Delta G_{\text{des}}^{Ni(OH)_2}$.

This definition allows us to calculate the Gibbs free energy of the reaction of interest,

$$\Delta G_{\tilde{R}} = \Delta G_{\text{ads}}^{H_2O} + \Delta G_R - \Delta G_{\text{ads}}^{H_2} + \Delta G_{\text{des}}^{Ni(OH)_2}$$
$$\Rightarrow \Delta G_R = 720\frac{\text{kJ}}{\text{mol}} - T \times 171\frac{\text{J}}{\text{K mol}}. \tag{F13}$$

The equilibrium constant of reaction (F12) is

$$\tilde{K} = e^{-[(\Delta G_R)/RT]} = \frac{\Theta_{Ni(OH)_2}^* \Theta_{H_2}^*}{(\Theta_{H_2O}^*)^2 \Theta_0^*}. \tag{F14}$$

The reaction occurs on the nickel surface, and the densities $\tilde{c}_i$ can therefore be interpreted as the surface coverage at equilibrium $\Theta_i^*$. The unoccupied surface coverage $\Theta_0^*$

represents the normalized nickel surface density at equilibrium. The equilibrium constant $\tilde{K}$ can now be used to calculate the reaction-rate constant $K$. As can be seen in Eq. (F14), the relations are nonlinear; thus, in order to avoid mathematical ambiguities, two special cases are examined.

(1) At equilibrium, the surface coverage of $Ni(OH)_2$ is dominant compared to the surface coverage of $H_2O$,

$$\frac{K}{k_{d,Ni(OH)_2}} \gg 1, \tag{F15}$$

as can be seen in Eq. (E5). Neglecting the terms proportional to $k_{d,Ni(OH)_2}/K$ in the expressions (E3) and (E4) yields

$$K = \frac{k_{a,H_2} k_{d,H_2O}}{2(2k_{a,H_2} + k_{a,H_2O})} \times \left( \sqrt{1 + \frac{4(2k_{a,H_2} + k_{a,H_2O})}{k_{a,H_2}(k_{d,H_2O})^2} k_{d,Ni(OH)_2} \Theta_0 \tilde{K}(2k_j + k_{d,H_2})} - 1 \right),$$

$$\text{with} \quad \Theta_0 = \frac{2k_{d,Ni(OH)_2} k_{d,H_2} + k_{d,Ni(OH)_2} k_j + k_{d,H_2O} k_j - k_{a,H_2O} k_j}{k_{d,Ni(OH)_2}(2k_{a,H_2} + k_{a,H_2O} + 2k_{d,H_2} + k_j) + k_{a,H_2O} k_{d,H_2} + k_{a,H_2} k_j + k_{d,H_2O} k_j}. \tag{F16}$$

(2) At equilibrium, the surface coverage of $Ni(OH)_2$ is small compared to the surface coverage of $H_2O$,

$$\frac{K}{k_{d,Ni(OH)_2}} \ll 1. \tag{F17}$$

By setting $K = 0$ in Eq. (E4) and for $\Theta^*_{H_2}$ and $\Theta^*_{H_2O}$ in Eq. (E3), $K$ can be defined

$$K = \tilde{K} k_{d,Ni(OH)_2} \frac{k_{a,H_2O}(k_{d,H_2} + k_j) + k_{a,H_2} k_j}{k_{a,H_2}} \times \frac{(k_{d,H_2} + k_j)}{k_{a,H_2O} k_{d,H_2} + k_{a,H_2} k_{d,H_2O} + k_{d,H_2} k_{d,H_2O} + k_j(k_{a,H_2} + k_{a,H_2O} + k_{d,H_2O})}. \tag{F18}$$

Equations (F16) and (F18) have in common the fact that $K$ vanishes if the reaction (F12) is suppressed, which corresponds to $\tilde{K} \to 0$. If the desorption reaction-rate constant $k_{d,Ni(OH)_2}$ equals zero, $K$ vanishes, too. It is similar to the case of adsorption and desorption reaction-rate constants which are connected via the relation (F2). When the forward reaction rate equals zero, the backward reaction rate has to vanish and vice versa. With this aspect, the factor $K/k_{Ni(OH)_2}$ can be interpreted as a function of the equilibrium constant of the $Ni(OH)_2$ adsorption (production) and desorption reaction.

In both Eq. (F16) and Eq. (F18), the factor

$$k_{a,H_2O}(k_{d,H_2} + k_j) + k_{a,H_2} k_j \tag{F19}$$

appears and, if this factor is zero, the reaction-rate coefficient $K$ is zero as well. This implication is appropriate since, in that case, it holds that $k_{a,H_2O} = k_j = 0$, which implies that no $H_2O$ molecules are brought to the surface and, therefore, that the reaction (F12) cannot occur.

The calculation of the reaction-rate coefficient $K$ is implemented as follows: both Eq. (F16) and Eq. (F18) are performed, and the ratio $K/k_{Ni(OH)_2}$ is calculated afterward in order to decide whether the influence of $Ni(OH)_2$ is small or large. Knowing the strength of the influence allows a choice of the corresponding equation. When all reaction-rate coefficients are determined, the surface coverage can be calculated [Eqs. (E3) and (E4)]. This knowledge allows an evaluation of the surface-diffusion coefficient $D_s$ [Eq. (13)].

## APPENDIX G: DESCRIPTION OF THE ARDELL THEORY

Many theories on the Ostwald ripening suffer from the disadvantage that they are only valid if the volume fraction of the regarded species $rV$ is vanishing small. A theory which takes into account a nonvanishing volume fraction is the Ardell (MLSW) theory [40]. In this theory, the time constant $K_O$ is given by

$$K_O = D_c c_e \frac{6\gamma V_{mol}^2 \rho^3}{\nu RT}, \tag{G1}$$

$$\rho = \frac{\sqrt{\beta^2 + \beta + 1} - 1 + \beta}{\beta}, \tag{G2}$$

$$\nu = \frac{3\rho^2}{1 + 2\beta\rho - \beta}, \tag{G3}$$

$$\beta = \frac{6rV^{1/3}}{e^{3rV}\Gamma(rV)}, \tag{G4}$$

$$\Gamma(rV) = \int_{8rV}^{\infty} x^{-(2/3)} e^{-x} dx. \tag{G5}$$

The variable $c_e$ denotes the concentration at equilibrium at a planar interface. It can be expressed as the number of particles in the porous phase $n_{\mathrm{Ni(OH)_2}}$ divided by the volume of the porous phase $V_p$. The number of particles in the porous phase can be expressed as a product of the particles per site $\sigma_0$, the total area $A_{\mathrm{Ni}}^{\mathrm{tot}}$, the surface coverage of $\mathrm{Ni(OH)_2}$ $\Theta^*_{\mathrm{Ni(OH)_2}}$, and the equilibrium factor between the particles on the surface and in the porous phase $\exp\left(\Delta G_{\mathrm{des}}^{\mathrm{Ni(OH)_2}}/RT\right)$. If the volume of the porous phase is written as the product of the porosity $\varepsilon$ and the electrode volume $V_{\mathrm{elec}}$, the final statement reads

$$\begin{aligned} c_e &= \frac{n_{\mathrm{Ni(OH)_2}}}{V_p} = \frac{\Theta^*_{\mathrm{Ni(OH)_2}} \sigma_0 A_{\mathrm{Ni}}^{\mathrm{tot}} e^{\Delta G_{\mathrm{des}}^{\mathrm{Ni(OH)_2}}/RT}}{\varepsilon V_{\mathrm{elec}}} \\ &= 3\Theta^*_{\mathrm{Ni(OH)_2}} \sigma_0 \left(e^{\Delta G_{\mathrm{des}}^{\mathrm{Ni(OH)_2}}/RT}\right) \frac{rV_{\mathrm{Ni}}}{r_{\mathrm{Ni}}\varepsilon}, \end{aligned} \tag{G6}$$

where Eq. (F8) is used.

## APPENDIX H: DERIVATION OF THE DIFFUSION CONSTANTS

By dividing the flow rate by the volume of the porous phase of the electrode $V_p = \varepsilon V_{\mathrm{elec}}$, a measure for the influence of the flow rate on the atmosphere can be defined:

$$D_{\mathrm{Ost}}^{\mathrm{fr}} \propto \frac{\dot{V}}{\varepsilon V_{\mathrm{elec}}}. \tag{H1}$$

Since the term on the right-hand side has a dimension of $1/\mathrm{h}$ and the term on the left-hand side a dimension of $\mathrm{m^2/s} = 3600\ \mathrm{m^2/h}$, the proportional constant has the dimension of an area $A_{\mathrm{eff}}$

$$D_{\mathrm{Ost}}^{\mathrm{fr}} := A_{\mathrm{eff}} \frac{\dot{V}}{\varepsilon V_{\mathrm{elec}}}. \tag{H2}$$

In general, the diffusion processes in a SOC electrode are more complicated. For example, if the pore size is smaller than the mean free path, the Knudsen diffusion has to be consulted and if an internal reforming reaction occurs, the gas will change its composition. The influence of these effects can be found in the literature [53–58].

As was discussed in Sec. II, the Ostwald ripening due to the deviation of the particle size takes the form

$$D_{\mathrm{Ost}}^{\mathrm{der}} = D_{\mathrm{Ost}}^{\mathrm{der},0} \frac{\sigma_r}{r_{\mathrm{Ni}}} \frac{r_{YSZ}}{r_{\mathrm{Ni}}}, \tag{H3}$$

where $D_{\mathrm{Ost}}^{\mathrm{der},0}$ is a proportional constant. Combining the two discussed mechanisms [Eqs. (H2) and (H3)] yields

$$D'_{\mathrm{Ost}} = A_{\mathrm{eff}} \frac{\dot{V}}{\varepsilon V_{\mathrm{elec}}} + D_{\mathrm{Ost},0}^{\mathrm{der}} \frac{\sigma_r}{r_{\mathrm{Ni}}} \frac{r_{YSZ}}{r_{\mathrm{Ni}}}. \tag{H4}$$

The diffusion coefficient in the Ostwald ripening $D_{\mathrm{Ost}}$ is assumed to be proportional to the pressure of $\mathrm{Ni(OH)_2}$ in the electrode $p_{\mathrm{Ni(OH)_2}}$. It can be expressed with the help of the Gibbs energy of the corresponding desorption reaction (Appendix F),

$$\frac{p^*}{p_0} = e^{-(\Delta G_{\mathrm{des}}/RT)}. \tag{H5}$$

This pressure has to be normalized to the partial pressure of the involved particles, i.e., $H_2$, $H_2O$, and $\mathrm{Ni(OH)_2}$. The pressure $p_{\mathrm{Ni(OH)_2}}$ will be an order of magnitude smaller than $p_{\mathrm{H_2}}$ and $p_{\mathrm{H_2O}}$, which are determined by the operating conditions and thus will not contribute significantly to the sum of the partial pressure. This sum will usually equal the total pressure $p_0$, but in cases where the fuel is diluted with nitrogen, the sum can become much smaller than $p_0$. The final expression for the diffusion coefficient is

$$D_{\mathrm{Ost}} = \frac{p_{\mathrm{Ni(OH)_2}}}{p_{\mathrm{H_2}} + p_{\mathrm{H_2O}}} \left( A_{\mathrm{eff}} \frac{\dot{V}}{\varepsilon V_{\mathrm{elec}}} + \frac{\sigma_r}{r_{\mathrm{Ni}}} \frac{r_{YSZ}}{r_{\mathrm{Ni}}} D_{\mathrm{Ost},0}^{\mathrm{der}} \right). \tag{H6}$$

## APPENDIX I: CLARIFICATION OF THE FREE PARAMETERS

The time constant $m$ is defined in Eqs. (9) and (13) as

$$m = \frac{D_s}{l^2}, \qquad D_s = D_{s,0}(1-\theta) e^{2\lambda_2(1-\Theta) + \sum_{i=0}^{n} \Gamma_i \Theta_i}. \tag{I1}$$

The value of $D_{s,0}$ is indicated in the literature [59] as

$$D_{s,0} = 24 \times e^{-(178.5\ \mathrm{kJ}/RT)} \times \frac{\mathrm{cm^2}}{\mathrm{s}}. \tag{I2}$$

The parameters $\lambda_2$, $\Gamma_i$ depend on the temperature, the surface structure, and the kind of molecules which are adsorbed. The parameters are proportional to

$$\lambda_2, \qquad \Gamma_i \propto \frac{RT\sigma_0}{\gamma}. \tag{I3}$$

The sites per unit $\sigma_0$ are incorporated in a way that the chemical potential $\mu$ vanishes if no sites are available ($\sigma_0 \to 0 \Rightarrow \mu \to 0$). An analysis of the dimensions produces a term of the dimension $\mathrm{J/m^2}$, which indicates as a

constant the surface tension of nickel $\gamma = 1.9\ \mathrm{J/m^2}$ [59]. As variables, which distinguish the different species in the atmosphere, $H_2$, $H_2O$, and $Ni(OH)_2$, the saturation pressures are suitable. The saturation pressure indicates the equilibrium between a species on the nickel surface and in the atmosphere in the electrode. The values of the Gibbs energies are listed in Appendix F. Obviously, a small energy barrier for leaving the surface corresponds to a high saturation pressure. A small energy barrier indicates that the binding of a molecule on the surface is not strong and that it will not contribute significantly to the energy-related chemical potential of the layer $\mu$. Thus, the saturation pressure is connected to the parameter $\Gamma_i$ in this way,

$$\Gamma_i \propto \frac{p_0}{p^*}. \tag{I4}$$

The parameter $\lambda_2$ relates the Ni coverage to $\mu$. The reservoir of Ni is the bulk region of the particle and not the surrounding gas atmosphere. That is why it is not expedient to expect a connection to the saturation pressure of Ni. There is no energy barrier (or at least only a very small one compared to the energy barrier of the adsorption and desorption reactions) to pass from the bulk to the surface. It is assumed that a factor similar to that in Eq. (I4) will be close to 1. This assumption allows us to rewrite Eq. (I3) as

$$\lambda_2 = c\frac{RT\sigma_0}{\gamma}, \qquad \Gamma_i = c\frac{RT\sigma_0}{\gamma}\frac{p_0}{p^*}. \tag{I5}$$

The dimensionless constant $c$ has no atmospheric dependencies, but it can be connected to microstructural parameters. If the porosity $\varepsilon$ vanishes, there will be no surface connected to the atmosphere and $\mu$ must disappear:

$$c = c(b,\varepsilon) = c_0 f(b) g(\varepsilon), \quad \text{with} \quad g(0) = 0. \tag{I6}$$

If $c$ has no dependency on $b$, $b \to 0$ would lead to a constant particle size $y = 1$ for all $t$'s [Eqs. (B11) and (23)]. If the porosity is nonzero, however, the size can differ from the initial size. This fact can be achieved by setting

$$c \propto \frac{1}{b}. \tag{I7}$$

A vanishing $b$ leads to a relative volume of

$$y = e^{c_0 g(\varepsilon) F(\Theta_i, x)}, \tag{I8}$$

where the functional dependencies on the surface coverage $\Theta_i$ and on the atmospheric parameters $x$, e.g., the temperatures $T$, are summarized in the function $F$. The Ni size will be constant only if the porosity vanishes, too. The simplest way to define $g(\varepsilon)$ is $g(\varepsilon) = \varepsilon$, but this is not sufficient. Regarding the special case $rV_{\mathrm{Ni}} = 0.5 \Rightarrow rV_{YSZ} = 0.5 - \varepsilon$, $r_{\mathrm{Ni}} = r_{YSZ}$, and letting $\varepsilon \to 0$ reveals

$$c \propto \frac{\varepsilon}{b} \propto \frac{\varepsilon}{\ln\left(\frac{V_0}{V_{YSZ}}\frac{rV_{\mathrm{Ni}}}{rV_{YSZ}}\right)} = \frac{\varepsilon}{\ln(1-2\varepsilon)} \overset{\varepsilon\to 0}{\to} \frac{1}{2}. \tag{I9}$$

Obviously, the surface energy is nonzero even for a vanishing porosity. In order to guarantee the discussed behavior, the function $g(\varepsilon)$ is set to

$$g(\varepsilon) = \varepsilon^2. \tag{I10}$$

This fixing determines the factor $c$ to be

$$c = c_0 \frac{\varepsilon^2}{b}. \tag{I11}$$

A remark on the expression in Eq. (I8) is necessary. Formula (I8) suggests that, in a case where $b \to 0$ and $\varepsilon \neq 0$, the volume jumps instantaneously from $y = 1$ to $y = \exp[c_0\varepsilon^2 F(\Theta_i, x)] > 1$. This nonphysical behavior results from the assumption made in Appendix E that the surface coverage is always at equilibrium. In fact, this is not the case when the experiment starts and the $H_2/H_2O$ partial pressures are set to the operational values. In Ref. [60], it is demonstrated that the time scale of the surface reactions is an order of magnitude smaller than the time scale of the agglomeration process. Nevertheless, the time scale is nonzero and a complete inclusion of the reaction mechanism would give the correct time evolution of the surface coverage, and a smooth time evolution of the nickel size is therefore restored.


[1] S. Foit, R.-A. Eichel, L. G. J. de Haart, and I. Vinke, Power-to-syngas—An enabling technology for the transition of the energy system? Production of tailored synfuels and chemicals using renewably generated electricity, Angew. Chem., Int. Ed. Engl., DOI: 10.1002/anie.201607552 (2016).

[2] S. Y. Gómez and D. Hotza, Current developments in reversible solid oxide fuel cells, Renewable Sustainable Energy Rev. **61**, 155 (2016).

[3] M. A. Laguna, Recent advances in high temperature electrolysis using solid oxide fuel cells: A review, J. Power Sources **203**, 4 (2012).

[4] P. Holtappels and R. Steinberger-Wilckens, Realising reliable, durable, energy efficient and cost effective SOFC systems (Real-SOFC), Fuel Cells **9**, 783 (2009).

[5] P. Mocoteguy and P. Brisse, A review and comprehensive analysis of degradation mechanisms of solid oxide electrolysis cells, Int. J. Hydrogen Energy **38**, 15887 (2013).

[6] A. Atkinson, S. Barnett, R. J. Gorte, J. T. S. Irvine, A. J. McEvoy, M. Mogensen, S. C. Singhal, and J. Vohs, Advanced anodes for high-temperature fuel cells, Nat. Mater. **3**, 17 (2004).

[7] M. S. Khan, S. B. Lee, R. H. Song, J. W. Lee, T. H. Lim, and S. J. Park, Fundamental mechanisms involved in the

degradation of nickel-yttria stabilized zirconia (Ni-*YSZ*) anode during solid oxide fuel cells operation: A review, Ceram. Int. **42**, 35 (2016).

[8] C. Chatzichristodoulou, M. Chen, P. V. Hendriksen, T. Jacobsen, and M. B. Mogensen, Understanding degradation of solid oxide electrolysis cells through modeling of electrochemical potential profiles, Electrochim. Acta **189**, 265 (2016).

[9] A. Faes, A. Hessler-Wyser, D. Presvytes, C. Vayenas, and J. van Herle, Nickel-zirconia anode degradation and triple phase boundary quantification from microstructural analysis, Fuel Cells **9**, 841 (2009).

[10] P. Tanasini, M. Cannarozzo, P. Costamagna, A. Faes, J. van Herle, A. Hessler-Wyser, and C. Comninellis, Experimental and theoretical investigation of degradation mechanisms by particle coarsening in SOFC electrodes, Fuel Cells **9**, 740 (2009).

[11] R. Vaßen, D. Simwonis, and D. Stöver, Modeling of the agglomeration of Ni-particles in anodes of solid oxide fuel cells, J. Mater. Res. **36**, 147 (2001).

[12] D. Kennouche, Y. K. Chen-Wiegart, C. Riscoe, J. Wang, and S. A. Barnett, Combined electrochemical and x-ray tomography study of the high temperature evolution of nickel ytrria stabilized zirconia solid oxide fuel cell anodes, J. Power Sources **307**, 604 (2016).

[13] H. N. Ch'ng and J. Pan, Sintering of particles of different sizes, Acta Mater. **55**, 813 (2007).

[14] J. S. Chappell, T. A. Ring, and J. D. Birchall, Particles size distribution effects on sintering rates, J. Appl. Phys. **60**, 383 (1986).

[15] F. Wakai and K. A. Brakke, Tensor virial equation of evolving surfaces in sintering of aggregates of particles by diffusion, Acta Mater. **61**, 4103 (2013).

[16] H. Y. Chen, H. C. Yu, J. S. Cronin, J. R. Wilson, S. A. Barnett, and K. Thornton, Simulation of coarsening in three-phase solid oxide fuel cell anodes, J. Power Sources **196**, 1333 (2011).

[17] D. Yeon, P. Cha, and M. Grant, Phase field model of stress-induced surface instabilities: Surface diffusion, Acta Mater. **54**, 1623 (2006).

[18] J. Deng, A phase field model of sintering with direction-dependent diffusion, Mater. Trans., JIM **53**, 385 (2012).

[19] H. Leclerc and J. C. Gelin, Numerical modeling of solid state sintering using heterogenous packing and diffusion processes, J. Mater. Process. Technol. **143–144**, 891 (2003).

[20] A. Ioselevich, A. A. Kornyshev, and W. Lehnert, Degradation of solid oxide fuel cell anodes due to sintering of metal particles, J. Electrochem. Soc. **144**, 3010 (1997).

[21] B. K. Chakraverty, Grain size distribution in thin films—1. Conservative systems, J. Phys. Chem. Solids **28**, 2401 (1967).

[22] SOFC-Life, "Deliverables D1.2 and D1.3," 2013.

[23] *Gas Phase Chemical Reaction Systems*, edited by J. Wolfrum, H.-R. Volpp, R. Rannacher, and J. Warnatz, Springer Series in Chemical Physics Vol. 61 (Springer, New York, 1996).

[24] V. N. Kuzovkov, E. A. Kotomin, and G. Zvejnieks, Atomistic theory of mesoscopic pattern formation induced by bimolecular surface reactions between oppositely charged molecules, J. Chem. Phys. **135**, 224503 (2011).

[25] W. G. Bessler, J. Warnatz, and D. G. Goodwin, The influence of equilibrium potential on the hydrogen oxidation kinetics of SOFC anodes, Solid State Ionics **177**, 3371 (2007).

[26] M. Vogler, A. Bieberle-Hütter, L. Gauckler, J. Warnatz, and W. G. Bessler, Modelling study of surface reactions, diffusion, and spillover at a Ni/*YSZ* patterned anode, J. Electrochem. Soc. **156**, B663 (2009).

[27] N. M. Tikekar, T. J. Armstrong, and A. V. Virkar, Reduction and reoxidation kinetics of nickel-based SOFC anodes, J. Electrochem. Soc. **153**, A654 (2006).

[28] W. G. Bessler, S. Gewies, C. Willich, G. Schiller, and K. A. Friedrich, Spatial distribution of electrochemical performance in a segmented SOFC: A combined modeling and experimental study, Fuel Cells **10**, 411 (2010).

[29] K. Sasaki and J. Maier, Chemical surface exchange of oxygen on $Y_2O_3$-stabilized $ZrO_2$, Solid State Ionics **161**, 145 (2003).

[30] A. B. Anderson and E. Vayner, Hydrogen oxidation and proton transport at the Ni-zirconia interface in solid oxide fuel cell anodes: Quantum chemical predictions, Solid State Ionics **177**, 1355 (2006).

[31] A. Gorski, V. Yurkiv, D. Starukhin, and H.-R. Volpp, $H_2O$ chemisorption and $H_2$ oxidation on yttria-stabilized zirconia: Density functional theory and temperature-programmed desorption studies, J. Power Sources **196**, 7188 (2011).

[32] V. Yurkiv, A. Utz, E. Ivers-Tiffée, H.-R. Volpp, and W. G. Bessler, Elementary kinetic modeling and experimental validation of electrochemical CO oxidation on Ni/*YSZ* pattern anodes, Electrochim. Acta **59**, 573 (2012).

[33] V. Yurkiv, A. Gorski, W. G. Bessler, and H.-R. Volpp, Density functional theory study of heterogeneous CO oxidation over an oxygen-enriched yttria-stabilized zirconia surface, Chem. Phys. Lett. **543**, 213 (2012).

[34] E. S. Hecht, G. K. Gupta, H. Zhu, A. M. Dean, R. J. Kee, L. Maier, and O. Deutschmann, Methane reforming kinetics within a Ni-*YSZ* SOFC anode support, Appl. Catal., A **295**, 40 (2005).

[35] R. J. Kee, H. Zhu, and D. G. Goodwin, Solid-oxide fuel cells with hydrocarbon fuels, Proc. Combust. Inst. **30**, 2379 (2005).

[36] C. Kemball, E. K. Rideal, and E. A. Guggenheim, Thermodynamics of monolayers, Trans. Faraday Soc. **44**, 948 (1948).

[37] R. Stübner, Ph.D. thesis, Technische Universität Dresden, 2001 (in German).

[38] A. Hauch, M. Mogensen, and A. Hagen, Ni/*YSZ* electrode degradation studied by impedance spectroscopy—Effect of $p(H_2O)$, Solid State Ionics **192**, 547 (2011).

[39] A. Baldan, Review: Progress in Ostwald ripening theories and their applications to nickel-base superalloys, J. Mater. Sci. **37**, 2171 (2002).

[40] A. Ardell, The effect of volume fraction on particle coarsening: Theoretical considerations, Acta Metall. Mater. **20**, 61 (1972).

[41] R. Krishna and J. A. Wesselingh, The Maxwell-Stefan approach to mass transfer, Chem. Eng. Sci. **52**, 861 (1997).

[42] A. E. Kobryn, V. G. Morozov, I. P. Omelyan, and M. V. Tokarchuk, Enskog-Landau kinetic equation. Calculation of the transport coefficient for charged hard spheres, Physica (Amsterdam) **230A**, 189 (1996).

[43] S. Jiang, Sintering behavior of $Ni/Y_2O_3$-$ZrO_2$ cermet electrodes of solid oxide fuel cells, J. Mater. Sci. **38**, 3775 (2003).
[44] D. Simwonis, F. Tietz, and D. Stöver, Nickel coarsening in annealed Ni/8*YSZ* anode substrates for solid oxide fuel cells, Solid State Ionics **132**, 241 (2000).
[45] K. Y. Foo and B. H. Hameed, Insights into the modeling of adsorption isotherm systems, Chem. Eng. J. (Lausanne) **156**, 2 (2010).
[46] A. Malek and S. Farooq, Comparison of isotherm models for hydrocarbon adsorption on activated carbon, AIChE J. **42**, 3191 (1996).
[47] T. Panczyk, Sticking coefficient and pressure dependence of desorption rate in the statistical rate theory approach to the kinetics of gas adsorption. Carbon monoxide adsorption/desorption rates on the polycrystalline rhodium surface, Phys. Chem. Chem. Phys. **8**, 3782 (2006).
[48] C. A. Ward and M. Elmoselhi, Molecular adsorption at a well defined gas-solid interphase: Statistical rate theory approach, Surf. Sci. **176**, 457 (1986).
[49] H. Zhu, R. J. Kee, V. M. Janardhanan, O. Deutschmann, and D. G. Goodwin, Modeling elementary heterogeneous chemistry and electrochemistry in solid-oxide fuel cells, J. Electrochem. Soc. **152**, A2427 (2005).
[50] R. Weast, *Handbook of Chemistry and Physics* (CRC Press, Boca Raton, 1976).
[51] W. D. Halstead, A review of saturated vapour pressures and allied data for the principal corrosion products of iron, chromium, nickel and cobalt in flue gases, Corros. Sci. **15**, 603 (1975).
[52] G. R. Belaton and A. S. Jordan, The gaseous hydroxides of cobalt and nickel, J. Phys. Chem. **71**, 4114 (1967).
[53] W. Lehnert, J. Meusiger, and F. Thom, Modeling of gas transport phenomena in SOFC anodes, J. Power Sources **87**, 57 (2000).
[54] M. Cannarozzo, S. Grosso, G. Agnew, A. del Borghi, and P. Costamagna, Effects of mass transport on the performance of solid oxide fuel cells composite electrodes, J. Fuel Cell Sci. Technol. **4**, 99 (2007).
[55] W. G. Bessler, S. Gewies, and M. Vogler, A new framework for physically modeling of solid oxide fuel cells, Electrochim. Acta **53**, 1782 (2007).
[56] J. M. Zalc, S. C. Reyes, and E. Iglesia, The effects of diffusion mechanism and void structure on transport rates and tortuosity factors in complex porous structures, Chem. Eng. Sci. **59**, 2947 (2004).
[57] J. R. Kalnin, E. A. Kotomin, and J. Maier, Calculations of the effective diffusion coefficient for inhomogeneous media, J. Phys. Chem. Solids **63**, 449 (2002).
[58] J. H. Harding, Short-circuit diffusion in ceramics, Interface Sci. **11**, 81 (2003).
[59] P. S. Maiya and J. M. Blakely, Surface self-diffusion and surface energy of nickel, J. Appl. Phys. **38**, 698 (1967).
[60] L. Kröll, Ph.D. thesis, Rheinisch-Westfälische Technische Hochschule Aachen, 2016.